Supplementary Material (2) to accompany ***The Maxwell-Stefan Description of Mixture Diffusion in Nanoporous Crystalline Materials***

Characteristics of the Maxwell-Stefan Diffusivities $Đ_1$, $Đ_2$, and $Đ_{12}$ in Ordered Nanoporous Crystalline Materials

Rajamani Krishna*, Jasper M. van Baten

Van 't Hoff Institute for Molecular Sciences, University of Amsterdam, Science Park 904,

1098 XH Amsterdam, The Netherlands

CORRESPONDING AUTHOR *Tel +31 20 6270990; Fax: + 31 20 5255604;

email: r.krishna@uva.nl

Table of Contents

1. Preamble

In this second of two Supplementary Materials to accompany our article *The Maxwell-Stefan Description of Mixture Diffusion in Nanoporous Crystalline Materials*, we summarize, and analyse, published Molecular Dynamics (MD) simulation data for unary and binary mixture diffusion of a wide variety of guest species in ordered crystalline nanoporous materials. The MD data examined pertain to the M-S diffusivities, $Đ_1$, $Đ_2$, and $Đ_{12}$ for a wide variety of binary mixtures (H_2/CO_2, H_2/CH_4, CO_2/N_2, CH_4/CO_2, CH_4/C_2H_6, CH_4/C_3H_8, CH_4/nC_4H_{10}, Ne/Ar, H_2/Ar, CH_4/Ar, Ne/CO_2, Ar/Kr) in several different nanoporous host materials. Tables 1, and 2 provide some salient structural information on various materials considered here.

Our overall objective is to examine the various characteristics of the M-S diffusivities $Đ_1$, $Đ_2$, and $Đ_{12}$. Also, we provide estimation procedures for the exchange coefficient $Đ_{12}$, that quantify correlations.

2. Introduction

A wide variety of crystalline nanoporous materials is used in membrane separations and pressure swing adsorption (PSA) devices [1-8]. These materials include zeolites (crystalline aluminosilicates), metal-organic frameworks (MOFs), zeolitic imidazolate frameworks (ZIFs), covalent organic frameworks (COFs), periodic mesoporous organosilicas (PMOs), SBA-16, and MCM-41. The characteristic pore dimensions of these structures are either in the *micro*-porous (d_p < 2 nm), or *meso*-porous ranges (2 nm < d_p < 50 nm). Several types of channel topologies are encountered, including one-dimensional (1D) channels (e.g. AFI, MIL-47, MIL-53(Cr), MgMOF-74, NiMOF-74, and BTP-COF), intersecting channels (e.g. MFI, BEA, Zn(bdc)dabco), cavities with large windows (e.g. FAU, NaX, NaY, IRMOF-1, CuBTC), and cages separated by narrow windows (e.g. ZIF-8, LTA, CHA, DDR). Table 1 and Table 2 provide some salient structural information on various materials considered in this study.

In comparison to traditionally used porous materials such as zeolites, MOFs and ZIFs offer significantly higher surface areas and porosities. This is underscored in the data presented in Figure 1 for surface areas and pore volumes of some representative zeolites, MOFs and ZIFs. The commonly used zeolite, FAU-Si, for example, has a characteristic size (window aperture) of 7.4 Å, a pore volume of 0.33 cm^3/g, and a surface area of 980 m^2/g. The accessible pore volumes of MOFs are commonly in the 0.5 – 2 cm^3/g range. Furthermore, significantly higher surface areas are available with MOFs; for example MOF-177 has an area of 4800 m^2/g. The pore dimensions of MOFs are also often significantly larger; MgMOF-74 has one-dimensional hexagonal-shaped channels of approximately 11 Å diameter. In the ensuing discussions, we use the terminology "open" structures to describe materials that have high pore volumes.

For design and development of separation process it is necessary to have a reliable *quantitative* description of the diffusion of mixtures of guest molecules inside the porous materials. Mixture diffusion within nanoporous crystalline materials such as zeolites, and metal-organic frameworks (MOFs), is often strongly influenced by the extent to which the diffusivity of one species is *correlated* to that of its partner. Most commonly, the less-mobile species *slows* down its more mobile partner by not vacating an adsorption site quick enough for its more mobile partner to occupy that position. Such slowing-down effects, also termed *correlation effects*, are quantified by the exchange coefficient $Đ_{12}$ in the Maxwell-Stefan (M-S) diffusion formulation. With increasing concentrations of guest molecules inside the pores, the $Đ_{12}$ tends to decrease significantly, implying that correlation effects become increasingly important for separation processes operating at high pressures. The exchange coefficients $Đ_{12}$ are not accessible directly from experiments, and there is a need for developing reliable procedures for estimating $Đ_{12}$ for any given guest-mixture/host-material combination.

With the aid of a careful and comprehensive analysis of published experimental and molecular simulation data we aim to demonstrate the following.

(1) The "factoring out" of the thermodynamic corrections to the driving forces leads to easier interpretation and analysis of diffusivity data.

(2) The M-S diffusivity $Đ_i$ for an *n*-component mixture has the same value as that for unary diffusion, if the comparison is made at the same total pore concentration. This is a desirable and potent feature of the M-S formulations. For mixtures exhibiting strong hydrogen bonding, the M-S diffusivity $Đ_i$ for mixture diffusion cannot be identified with the value of the unary diffusivity.

(3) Two limiting scenarios for the *degree of correlations* can be identified: (a) negligible correlations: $Đ_i/Đ_{ij} \to 0$, and (b) dominant correlations: $Đ_i/Đ_{ij} \to \infty$. For each of these scenarios, simple expressions can be derived that are useful. The proper appreciation, and quantification, of correlation effects allows us to choose the proper material for a given separation application. In some cases, we should aim for materials with negligible degree of correlations; in others, materials that offer high degree of correlations are preferred.

(4) The M-S exchange coefficient $Đ_{ij}$, that quantifies correlations, can be related to the corresponding value of $Đ_{ij,fl}$ for the fluid mixture. For meso-porous materials, $Đ_{ij} \approx Đ_{ij,fl}$, when compared at the same total pore concentration c_t. For micro-porous materials, $Đ_{ij}$ is lower than the corresponding $Đ_{ij,fl}$, by a factor that depends on the pore topology and structure.

(5) We also examine the accuracy of the Vignes interpolation formula for estimation of the $Đ_{12}$ on the basis of unary diffusivity data.

1. The Maxwell-Stefan equations for *n*-component diffusion in nanoporous materials

The Maxwell-Stefan (M-S) equations provide the most convenient, and practical formulation of *n*-component diffusion inside porous crystalline materials; the M-S equations, that apply equally for micro- and meso-porous frameworks, can be written as [9-16]

$$-\phi\frac{c_i}{RT}\nabla\mu_i = \sum_{\substack{j=1\\ j\neq i}}^{n}\frac{x_j N_i - x_i N_j}{Đ_{ij}} + \frac{N_i}{Đ_i}; \quad i = 1,2,...n \tag{1}$$

where ϕ represents the fractional pore volume and the c_i are the concentrations, defined in terms of moles per m^3 of *accessible* pore volume, within the pore. It is to be noted that the ϕ appears in the M-S

equations (1) because the c_i are defined in terms of pore volume and not the total volume of the crystals. The fluxes N_i defined in equation (1) are expressed in terms of the number of moles of species *i* transported per second per m^2 of *crystalline material*, of which only a fraction ϕ is accessible to the guest molecules. The M-S equations (1) apply equally to meso-porous and micro-porous materials [15, 16]. In equation (1) the $Đ_i$ is the M-S diffusivities of species *i*, portraying the interaction between component *i* in the mixture with the surface, or wall of the structure. An important advantage of the M-S formulation is that the $Đ_i$ can be identified with the values for unary species *i*; there are however exceptional circumstances where this advantage does not hold [17, 18]. The $Đ_{ij}$ are M-S exchange coefficients representing interaction between component *i* with component *j*. At the molecular level, the $Đ_{ij}$ reflect how the facility for transport of species *i correlates* with that of species *j*.

The pore concentrations c_i are related to the more conventionally used molar loadings q_i by the expression

$$c_i = \frac{\rho q_i}{\phi} = \frac{q_i}{V_p} \tag{2}$$

where ρ represents the framework density, and V_p is the m^3 accessible pore volume per kg of framework. The c_i are useful measures when comparing different materials. We will have occasion to use both c_i and the molar loadings q_i.

An equivalent formulation of the M-S equations uses the molar loadings q_i as concentration measures

$$-\rho \frac{q_i}{RT} \nabla \mu_i = \sum_{\substack{j=1 \\ j \neq i}}^{n} \frac{x_j N_i - x_i N_j}{Đ_{ij}} + \frac{N_i}{Đ_i}; \quad i = 1,2,..n \tag{3}$$

in which the M-S diffusivities, $Đ_i$ and $Đ_{ij}$, have the same significance, and magnitudes as in equations (1).

The x_i in equations (1) and (3) represent the component mole fractions in the adsorbed phase within the pores

$$x_i = q_i / q_t = \quad c_i / c_t; \quad 1,2,.....n \tag{4}$$

where q_t and c_t are the *total* mixture loadings and pore concentrations, respectively:

$$q_t = \sum_{i=1}^{n} q_i; \quad c_t = \sum_{i=1}^{n} c_i \tag{5}$$

The Onsager reciprocal relations require

$$Đ_{ij} = Đ_{ji} \tag{6}$$

The chemical potential gradients $\nabla\mu_i$ can be related to the gradients in the pore concentrations, c_i, and the gradients of the molar loadings, q_i, by defining thermodynamic correction factors Γ_{ij}

$$\frac{q_i}{RT}\nabla\mu_i = \sum_{j=1}^{n}\Gamma_{ij}\nabla q_j; \quad \frac{c_i}{RT}\nabla\mu_i = \sum_{j=1}^{n}\Gamma_{ij}\nabla c_j; \quad \Gamma_{ij} = \frac{q_i}{p_i}\frac{\partial p_i}{\partial q_j} = \frac{c_i}{p_i}\frac{\partial p_i}{\partial c_j}; \quad i,j = 1,....n \tag{7}$$

By defining an n-dimensional square matrix $[B]$ with elements

$$B_{ii} = \frac{1}{Đ_i} + \sum_{\substack{j=1 \\ j\neq i}}^{n}\frac{x_j}{Đ_{ij}}; \qquad B_{ij} = -\frac{x_i}{Đ_{ij}}; \quad i,j = 1,2....n \tag{8}$$

we can recast equation (3) into the following form

$$-\rho\frac{q_i}{RT}\nabla\mu_i = -\phi\frac{c_i}{RT}\nabla\mu_i = \sum_{j=1}^{n}B_{ij}N_j; \quad i = 1,2,..n \tag{9}$$

Equation (9) can be re-written in n-dimensional matrix notation as

$$(N) = -\rho[B]^{-1}[\Gamma]\nabla(q) = -\phi[B]^{-1}[\Gamma]\nabla(c) \tag{10}$$

We denote the inverse of $[B]$ as $[\Delta]$:

$$[B]^{-1} \equiv [\Delta] \tag{11}$$

The elements Δ_{ij} can be determined from MD simulations in each of the three coordinate directions using the formula

$$\Delta_{ij} = \frac{1}{2}\lim_{\Delta t\to\infty}\frac{1}{n_j}\frac{1}{\Delta t}\left\langle\left(\sum_{l=1}^{n_i}\left(\mathbf{r}_{l,i}(t+\Delta t)-\mathbf{r}_{l,i}(t)\right)\right)\bullet\left(\sum_{k=1}^{n_j}\left(\mathbf{r}_{k,j}(t+\Delta t)-\mathbf{r}_{k,j}(t)\right)\right)\right\rangle \tag{12}$$

In this expression n_i and n_j represent the number of molecules of species *i* and *j* respectively, and $\mathbf{r}_{l,i}(t)$ is the position of molecule *l* of species *i* at any time *t*. The Onsager reciprocal relations (6) translate to

$$\Delta_{ij}c_j = \Delta_{ji}c_i; \quad \Delta_{ij}q_j = \Delta_{ji}q_i \tag{13}$$

Before examining the characteristics of M-S diffusivities in nanoporous materials, let us consider the special case of diffusion in fluid phase mixtures.

2. M-S diffusivities for diffusion in fluid phase mixtures

The use of the pore concentrations c_i in equation (1) is particularly convenient for estimation of the exchange coefficients $Đ_{ij}$. To appreciate this, let us consider the limiting case of *n*-component mixture diffusion in the absence of any interactions with the pore walls. In this case, we have $\phi = 1$, and equation (1) degenerates to the equation for describing bulk fluid phase mixture diffusion [19]

$$-\frac{c_i}{RT}\nabla\mu_i = \sum_{\substack{j=1\\ j\neq i}}^{n}\frac{x_jN_i - x_iN_j}{Đ_{ij,fl}}; \quad i = 1,2,...n; \quad \text{bulk fluid mixture} \tag{14}$$

where $Đ_{ij,fl}$ represents the M-S diffusivity for the binary pair *i-j* in the *n*-component fluid mixture. For bulk fluid phase mixtures, the chemical potential gradients satisfy the Gibbs-Duhem relationship

$$\sum_{i=1}^{n}x_i\nabla\mu_i = 0 \tag{15}$$

and so only *n*-1 of the equations (14) are independent.

For a binary fluid phase mixture, equations (14) simplifies to yield just one independent equation

$$-\frac{c_1}{RT}\nabla\mu_1 = -c_t\left(1+\frac{\partial\ln\gamma_1}{\partial\ln x_1}\right)\nabla x_1 = -c_t\Gamma_1\nabla x_1 = \frac{x_2N_1 - x_1N_2}{Đ_{12,fl}} \tag{16}$$

which can be recast into the form

$$N_1 - x_1\left(N_1 + N_2\right) = -\frac{c_1}{RT} Đ_{12,fl} \nabla \mu_1 = -c_t Đ_{12,fl} \Gamma_1 \nabla x_1 \tag{17}$$

The Fick diffusivity for binary fluid mixtures is related to the corresponding M-S diffusivity

$$D_{12,fl} = Đ_{12,fl} \Gamma_1 \tag{18}$$

It is to be noted that for binary fluid mixtures, the Fick and M-S diffusivities are defined in terms of fluxes defined with respect to the molar average reference velocity.

For highly non-ideal liquid mixtures, because of the strong composition dependence of the thermodynamic factor $\Gamma_1 = \left(1 + \frac{\partial \ln \gamma_1}{\partial \ln x_1}\right)$, we should expect the Fick diffusivity to also exhibit a corresponding strong composition dependence; this is indeed borne out by experimental data of Clark and Rowley [20] for the system methanol (1) – *n*-hexane for which we note that the Fick diffusivity tends to approach zero in the region of the phase transition point near $x_1 \approx 0.5$; see Figure 2a. The Maxwell-Stefan diffusivity, calculated from the experimental Fick diffusivity data using equation (18), shows a relatively mild dependence on mixture composition. The experimental data of Clark and Rowley [20] are in reasonably good agreement with the MD simulations of Krishna and van Baten [21]; see Figure 2b.

For a fluid phase mixture, the Vignes [22, 23] interpolation formula is commonly used in practice for estimation of the $Đ_{12,\mathrm{fl}}$

$$Đ_{12,fl} = \left(Đ_{11,fl}\right)^{x_1} \left(Đ_{22,fl}\right)^{x_2} \tag{19}$$

where the $Đ_{\mathrm{ii,fl}}$ represent the self-exchange coefficients, or self-diffusivities, for *unary* fluid phase diffusion. The Vignes relation (19) implies that the logarithm of $Đ_{12,\mathrm{fl}}$ should be linear in the mole fraction x_1. From the data in Figure 2 we see that this empirical model of Vignes holds reasonably well. The factoring-out of the influence of mixture thermodynamics, is the root cause of the well-behaved characteristics of the M-S diffusivity $Đ_{12,\mathrm{fl}}$.

Further validation of the Vignes interpolation formula (19) is demonstrated in Figure 3 for six different equimolar fluid mixtures. Reliable procedures for estimation of $Đ_{12,\mathrm{fl}}$ from molecular properties of the individual species are available in the literature; for further information regarding the estimation of the Maxwell-Stefan diffusivity for gaseous and liquid mixtures, the reader is referred to Taylor and Krishna [24] and Wesselingh and Krishna [25]. The dashed lines in Figure 3 show the estimations of $Đ_{12,\mathrm{fl}}$ using the method of Fuller, Schettler and Giddings (FSG) [26], developed for *ideal gas* mixtures. We note that for concentrations $c_\mathrm{t} < 6$ kmol m^{-3}, the MD simulated $Đ_{12,\mathrm{fl}}$ values are in excellent agreement with the FSG estimations. For concentrations $c_\mathrm{t} > 6$ kmol m^{-3}, the $Đ_{12,\mathrm{fl}}$ values reflect those in dense condensed fluids, for which some estimation procedures are also available in the literature [27].

We aim to show that estimations of $Đ_{12,\mathrm{fl}}$ provide a good starting point for estimation of the corresponding $Đ_{12}$ in nanporous materials. We start with unary diffusion in nanoporous structures.

3. Unary diffusivities and correlations

For unary diffusion, equation (1) simplifies to yield

$$-\phi\frac{c_i}{RT}\nabla\mu_i = \frac{N_i}{Đ_i} \tag{20}$$

The pure component $Đ_\mathrm{i}$ is obtained from MD simulations of molecular displacements using the formula in each of the coordinate direction

$$Đ_i = \frac{1}{2}\lim_{\Delta t\to\infty}\frac{1}{n_i}\frac{1}{\Delta t}\left\langle\left(\sum_{l=1}^{n_i}\left(\mathbf{r}_{l,i}(t+\Delta t)-\mathbf{r}_{l,i}(t)\right)\right)^2\right\rangle \tag{21}$$

In this expression n_i represents the number of molecules of species i, and $\mathbf{r}_{\mathrm{l,i}}(t)$ is the position of molecule l of species i at any time t.

There is no experimental procedure for direct determination of the $Đ_\mathrm{i}$. Transient uptake and chromatographic experiments yield the Fick diffusivity D_i, also termed "transport" diffusivity, that relates the flux N_i of species i to the gradient of the molar loadings, q_i, or pore concentration, c_i

$$N_i = -\rho D_i \nabla q_i = -\phi D_i \nabla c_i \tag{22}$$

where ϕ is the fractional pore volume. The D_i are related to the M-S diffusivities by the thermodynamic factor Γ_i

$$D_i = Đ_i \Gamma_i; \quad \Gamma_i \equiv \frac{c_i}{f_i}\frac{\partial f_i}{\partial c_i} = \frac{q_i}{f_i}\frac{\partial f_i}{\partial q_i} \tag{23}$$

The M-S diffusivity $Đ_i$ is often termed the "corrected" diffusivity because the formula (23) suggests that adsorption thermodynamic effects have been "factored out". The values of Γ_i can be determined by analytic differentiation of fits to the adsorption isotherms. For a proper understanding of the concentration dependence of the diffusivities, we need the isotherm fits to be good representations over the entire range of concentrations, and not just in the Henry regime ($c_i \to 0; \quad q_i \to 0$).

The self-exchange diffusivity, $Đ_{ii}$, is defined by applying the M-S equations (3) to a binary mixture, that consists of identical species, tagged and un-tagged and assuming, furthermore, that we have equimolar diffusion $N_1 + N_2 = 0$. In this special case, the M-S equations (3) can be used to derive the following relation between the self-diffusivity, $D_{i,self}$, and the M-S diffusivity, $Đ_i$, for *unary* diffusion [16]

$$-\phi\frac{c_1}{RT}\nabla\mu_1 = \frac{(x_1 + x_2)N_1}{Đ_{11}} + \frac{N_1}{Đ_1} = \left(\frac{1}{Đ_{11}} + \frac{1}{Đ_1}\right)N_1 \tag{24}$$

Equation (24) defines the self-diffusivity within a pore for this special situation

$$-\phi\frac{c_i}{RT}\nabla\mu_i = \frac{N_i}{D_{i.self}} \tag{25}$$

and so we derive the expression

$$\frac{1}{D_{i,self}} = \frac{1}{Đ_i} + \frac{1}{Đ_{ii}} \tag{26}$$

The self-diffusivities $D_{\mathrm{i,self}}$ is computed from MD simulations by analyzing the mean square displacement of each species i for each coordinate direction

$$D_{i,self} = \frac{1}{2n_i} \lim_{\Delta t \to \infty} \frac{1}{\Delta t} \left\langle \left(\sum_{l=1}^{n_i} \left(\mathbf{r}_{l,i}(t + \Delta t) - \mathbf{r}_{l,i}(t) \right)^2 \right) \right\rangle \tag{27}$$

Equation (26) has been used to determine the self-exchange diffusivities $Đ_{\mathrm{ii}}$ from MD simulated $D_{\mathrm{i,self}}$ and $Đ_{\mathrm{i}}$ for unary diffusion. The self-exchange diffusivity, $Đ_{\mathrm{ii}}$, quantifies the extent of correlations for unary diffusion. The $Đ_{\mathrm{i}}$, reflecting *collective* motion of molecules (cf. eqn (21)), is free from such correlation effects; it is for this reason that the $Đ_{\mathrm{i}}$ are amenable to simpler interpretation, and modeling, than the $D_{\mathrm{i,self}}$. The Fick diffusivity, determined from say uptake or chromatographic experiments [1], is *directly* influenced by adsorption thermodynamics and is therefore much more difficult to interpret from a fundamental viewpoint than the M-S $Đ_{\mathrm{i}}$.

For CH_4, as illustration, MD simulations of the values of $D_{\mathrm{i,self}}$, $Đ_{\mathrm{i}}$, along with the $Đ_{\mathrm{ii}}$ calculated using Equation (26), are shown in Figure 4 for six different host structures. At any pore concentration, $D_{\mathrm{i,self}} \leq Đ_{\mathrm{i}}$; this is because individual jumps of molecules are *correlated* due to re-visitation of sorption sites that have been recently vacated. The extent of correlations is captured by the self-exchange coefficient $Đ_{\mathrm{ii}}$. For all structures, in the limit of low pore concentrations, $c_i \to 0$; $q_i \to 0$, molecule-molecule interactions are of negligible importance, and $Đ_{\mathrm{ii}}$ is significantly higher than $D_{\mathrm{i,self}}$ and $Đ_{\mathrm{i}}$. Correlations become increasingly significant as the pore concentrations are increased, and this is evidenced by the observation that $Đ_{\mathrm{ii}}$ decreases more sharply with increasing c_{i}, than the M-S diffusivity $Đ_{\mathrm{i}}$. As pore saturation conditions are approached, the diffusion characteristics are dominated by correlation effects [28, 29].

The relative importance of molecule-wall and molecule-molecule interactions is different for each structure. In meso-porous materials, the self-exchange coefficient $Đ_{\mathrm{ii}}$ can be identified with the self-diffusivity in the *fluid* phase, $Đ_{\mathrm{ii,fl}}$, over the entire range of pore concentrations [16]. This is demonstrated by the data for BTP-COF that has 1D hexagonal-shaped channels of 34 Å size; see Figure 4f. For BTP-COF we note that $Đ_{\mathrm{ii}} \approx Đ_{\mathrm{ii,fl}}$

$$\frac{1}{D_{i,self}} = \frac{1}{Đ_i} + \frac{1}{Đ_{ii,fl}}; \quad \text{Bosanquet formula} \tag{28}$$

over the entire range of concentrations; this conclusion is valid for all guest molecules in meso-porous channels [15, 16, 30, 31]. The expression (28), with the Knudsen formula used for $Đ_i$, was developed by Bosanquet in a classified report dated September 27, 1944, and this interpolation formula only became known when it was later cited by Pollard and Present [32]; see also Krishna and van Baten [31].

Correlations are relatively weak for LTA-5A in which the diffusivities are largely dictated by hopping of molecules, one-at-a-time, across 4 Å × 4.58 Å size windows; this is evidenced by the fact that $D_{i,self} \approx Đ_i$ for $c_i < 20$ kmol m^{-3}; see Figure 4c. Correlations in LTA-5A become of importance only at higher pore concentrations; these conclusions are also valid for other cage-type structures such as CHA, DDR, ITQ-29, ERI, and ZIF-8 [13, 33].

The self-exchange $Đ_{ii}$ were determined for several guest/host combinations from unary MD simulations. In each case the $Đ_{ii}$ is also a fraction, $F \equiv Đ_{ii}/Đ_{ii,fl}$, of the corresponding value of the fluid phase $Đ_{ii,fl}$; see data in Figure 5 for some selected guest/host combinations. For micro-porous materials, the values of $Đ_{ii}$ are lower than $Đ_{ii,fl}$ by a factor F; this factor is practically constant over the entire range of pore concentrations [16, 33].

Generally speaking, the more "open" the structure, the closer is the value of F to unity. Conversely, for structures in which the structures are strongly confined, the fraction F is significantly below unity. The extent of lowering depends on pore size, pore topology and connectivity. In MFI zeolite, the factor $F \approx 0.1$. For MgMOF-74, NaX, and IRMOF-1, the factor F falls in the range 0.4 – 0.7. Figure 6 presents a plot of the F plotted against the pore volume of the porous host structures, V_p. The correlation is not perfect, suggesting that other aspects such as channel dimensions, and pore connectivity are also determinants of the exchange coefficient $Đ_{ii}$.

Generally speaking, we have $\Gamma_i \geq 1$, i.e. $1/\Gamma_i < 1$, resulting in the hierarchy of diffusivities $D_{i,self} \leq Đ_i \leq D_i$ as witnessed in the six examples shown in Figure 4. In cases where molecular clustering occurs we

have $1/\Gamma_i > 1$ for a range of pore concentrations; this results in a hierarchy of diffusivities $D_{i,self} \leq Đ_i \geq D_i$ [11, 12, 17, 34]. Hydrogen bonding manifests for guest molecules such as water and alcohols, and in regions where cluster formation occurs we have $1/\Gamma_i > 1$. The characteristic signature of cluster formation is that the adsorption isotherm exhibits a steep increase in the loading. Figure 7a illustrates the steepness of the isotherms for methanol and ethanol adsorption isotherms within the cages of ZIF-8. The steepness of the isotherms can be properly captured provided by using the dual-site Langmuir-Freundlich isotherm

$$q_i = q_{i,A,sat} \frac{b_{i,A} f_i^{\nu_{i,A}}}{1 + b_{i,A} f_i^{\nu_{i,A}}} + q_{i,B,sat} \frac{b_{i,B} f_i^{\nu_{i,B}}}{1 + b_{i,B} f_i^{\nu_{i,B}}} \tag{29}$$

with at least one of the exponents ν_i exceeds unity; the fits are shown by the continuous solid lines. Analytic differentiation of the isotherm fits are used to determine the inverse thermodynamic correction factors $1/\Gamma_i > 1$, that are plotted in Figure 7b as a function of the loading within the cages. The inverse thermodynamic factor exceeds unity, i.e. $1/\Gamma_i > 1$, for a range of pore concentrations where clustering manifests. The experimental data on diffusivities of methanol and ethanol in ZIF-8 confirms the unusual hierarchy $D_{i,self} \leq Đ_i \geq D_i$ for the range of concentrations where clusters form; see Figure 8.

When the temperature T is lower than the critical temperature, T_c, the adsorbed phase is in a meta-stable thermodynamic state, and this leads to the possibility of cluster formation. Figure 9 shows the experimental data of the Fick diffusivity for (a) neopentane (neo-P, T_c = 434 K) and (a) 2-methylbutane (2MB, T_c = 460 K) in CuBTC, determined at T = 298 K using transient uptake monitored by Infra-Red Microscopy [35].

The thermodynamic correction factor Γ_i attains values below unity for the range of loadings $20 < \Theta_i < 55$ molecules per unit cell, signifying clustering for this range of loadings. The deep valley in the Γ_i vs. Θ_i data results in a corresponding valley in the Fick D_i vs. Θ_i data. The loading dependence characteristics of the Fick D_i is analogous to that of the methanol - *n*-hexane liquid mixture (cf. Figure

2). Factoring out the thermodynamic corrections on the Fick D_i allows a simpler interpretation of the diffusivity characteristics [18, 35].

Further detailed discussions on the influence of molecular clustering on the loading dependences of diffusivities are available in earlier works [12, 17, 18, 34-40].

4. Degree of correlations

For the special case of binary mixture diffusion, equation (1) simplifies to

$$\begin{aligned} -\phi\frac{c_1}{RT}\nabla\mu_1 &= \frac{x_2N_1-x_1N_2}{Đ_{12}}+\frac{N_1}{Đ_1};\\ -\phi\frac{c_2}{RT}\nabla\mu_2 &= \frac{x_1N_2-x_2N_1}{Đ_{12}}+\frac{N_2}{Đ_2} \end{aligned} \tag{30}$$

we obtain the explicit expression for [Δ]

$$[\Delta]\equiv[B]^{-1}=\begin{bmatrix} \frac{1}{Đ_1}+\frac{x_2}{Đ_{12}} & -\frac{x_1}{Đ_{12}}\\ -\frac{x_2}{Đ_{12}} & \frac{1}{Đ_2}+\frac{x_1}{Đ_{12}} \end{bmatrix}^{-1} \tag{31}$$

The matrix inversion can be carried out explicitly to yield the following expression

$$[\Delta]\equiv[B]^{-1}=\frac{1}{1+\frac{x_1Đ_2}{Đ_{12}}+\frac{x_2Đ_1}{Đ_{12}}}\begin{bmatrix} Đ_1\left(1+\frac{x_1Đ_2}{Đ_{12}}\right) & \frac{x_1Đ_1Đ_2}{Đ_{12}}\\ \frac{x_2Đ_1Đ_2}{Đ_{12}} & Đ_2\left(1+\frac{x_2Đ_1}{Đ_{12}}\right) \end{bmatrix} \tag{32}$$

For a wide variety of guest/host combinations we used MD simulations to determine the four elements Δ_{11}, Δ_{12}, Δ_{21}, and Δ_{22} for a range of pore concentrations and using the formula (12).

As illustration, Figure 10 shows the MD simulated values of Δ_{ij} for equimolar binary $CO_2(1)/H_2(2)$ mixtures (c_1=c_2) in a variety of zeolites and MOFs, as a function of the total pore concentration c_t= c_1+c_2. Before examining in detail the procedures for estimating the elements Δ_{ij}, let us list some of the common characteristics.

In the limit of vanishingly small pore concentrations, $c_t = c_1 + c_2 \rightarrow 0$, $\Delta_{12} \rightarrow 0$, and $\Delta_{21} \rightarrow 0$. Also, $\Delta_{11} \rightarrow Đ_1$, $\Delta_{22} \rightarrow Đ_2$.

As the total pore concentration increases and approaches saturation, all Δ_{ij} converge to the same value.

In order to test the assumption that whether the M-S diffusivity $Đ_i$ is the same as the value for pure component we derive formulae for extracting $Đ_1$, $Đ_2$, from simulated values of the M-S matrix [Δ]. From equation (32) we derive

$$\frac{\Delta_{11}}{\Delta_{12}} = \frac{\left(1 + \frac{x_1 Đ_2}{Đ_{12}}\right)}{\frac{x_1 Đ_2}{Đ_{12}}}; \quad \frac{Đ_{12}}{x_1 Đ_2} = \left(\frac{\Delta_{11}}{\Delta_{12}} - 1\right) \tag{33}$$

and

$$\frac{\Delta_{22}}{\Delta_{21}} = \frac{\left(1 + \frac{x_2 Đ_1}{Đ_{12}}\right)}{\frac{x_2 Đ_1}{Đ_{12}}}; \quad \frac{Đ_{12}}{x_2 Đ_1} = \left(\frac{\Delta_{22}}{\Delta_{21}} - 1\right) \tag{34}$$

Combining equations (32), (33) and (34) we can derive the following explicit expressions for $Đ_1$, $Đ_2$, and $Đ_{12}$

$$Đ_1 = \frac{\Delta_{11}\left(1 + \frac{1}{\left(\frac{\Delta_{11}}{\Delta_{12}} - 1\right)} + \frac{1}{\left(\frac{\Delta_{22}}{\Delta_{21}} - 1\right)}\right)}{\left(1 + \frac{1}{\left(\frac{\Delta_{11}}{\Delta_{12}} - 1\right)}\right)} \tag{35}$$

$$Đ_2 = \frac{\Delta_{22}\left(1+\frac{1}{\left(\frac{\Delta_{11}}{\Delta_{12}}-1\right)}+\frac{1}{\left(\frac{\Delta_{22}}{\Delta_{21}}-1\right)}\right)}{\left(1+\frac{1}{\left(\frac{\Delta_{22}}{\Delta_{21}}-1\right)}\right)} \tag{36}$$

$$Đ_{12} = x_1\left(\frac{\Delta_{22}}{\Delta_{21}}-1\right)\frac{\Delta_{11}\left(1+\frac{1}{\left(\frac{\Delta_{11}}{\Delta_{12}}-1\right)}+\frac{1}{\left(\frac{\Delta_{22}}{\Delta_{21}}-1\right)}\right)}{\left(1+\frac{1}{\left(\frac{\Delta_{11}}{\Delta_{12}}-1\right)}\right)} = x_2\left(\frac{\Delta_{11}}{\Delta_{12}}-1\right)\frac{\Delta_{22}\left(1+\frac{1}{\left(\frac{\Delta_{11}}{\Delta_{12}}-1\right)}+\frac{1}{\left(\frac{\Delta_{22}}{\Delta_{21}}-1\right)}\right)}{\left(1+\frac{1}{\left(\frac{\Delta_{22}}{\Delta_{21}}-1\right)}\right)} \tag{37}$$

The value of $Đ_{12}$, relative to that of $Đ_1$, determines the extent to which the flux of species 1 is influenced by the chemical potential gradient of species 2. The larger the *degree of correlation*, $Đ_1/Đ_{12}$, the stronger is the influence of coupling. Generally speaking, the more-strongly-adsorbed-tardier partner species will have the effect of slowing down the less-strongly-adsorbed-more-mobile partner in the mixture. In order to understand the relative importance of correlations on the calculations of the fluxes for binary mixture diffusion, we define the degrees of correlation, $Đ_1/Đ_{12}$, and $Đ_2/Đ_{12}$. For values of $Đ_1/Đ_{12} > 1$, and $Đ_2/Đ_{12} > 1$, the first member on the right of M-S equations (30) contribute significantly to the fluxes and therefore correlations are significant. Conversely, for values of $Đ_1/Đ_{12} \to 0$, and $Đ_2/Đ_{12} \to 0$, the contribution of the first right member of M-S equations (30) can be ignored and correlations can be considered to be of negligible importance:

$$[\Delta] = \begin{bmatrix} Đ_1 & 0 \\ 0 & Đ_2 \end{bmatrix}; \quad N_i = -\phi Đ_i \frac{c_i}{RT}\nabla\mu_i; \quad \text{negligible correlations} \tag{38}$$

Figure 11 shows MD data on $Đ_1/Đ_{12}$ for diffusion of six different mixtures in a variety of host materials, expressed as a function of the total concentration, c_t, of the adsorbed mixture within the pores. The use of pore concentrations c_t rather than the molar loadings affords a fairer comparison of different host materials as explained in previous works [16]. For any guest/host combination, $Đ_1/Đ_{12}$ is seen to increase as the pore concentration increases; this implies that correlation effects are expected to be stronger for membrane separations operating at higher pressures. The degree of correlations is weakest in cage-type structures such as CHA, DDR and LTA; the reason is that the molecules jump one-at-a-time across the narrow windows separating adjacent cages; CO_2 molecules jump length-wise across the windows. At the other end of the spectrum, correlations are strongest in one-dimensional (1D) channel structures (e.g. NiMOF-74), intersecting channels (e.g. MFI), and "open" structures (e.g. IRMOF-1, FAU, NaX) consisting of large cages separated by wide windows.

5. Dominant correlations scenario for [Δ]

From the data in Figure 11 we also note that $Đ_1/Đ_{12}$ values significantly exceed unity as saturation conditions are approached. For the limiting scenario where correlations are dominant, described by $Đ_i/Đ_{12} \to \infty$, we can derive the following explicit expressions for the Δ_{ij}

$$\begin{aligned}
\Delta_{11} = \Delta_{12} &= \frac{c_1}{\frac{c_1}{Đ_1}+\frac{c_2}{Đ_2}} = \frac{q_1}{\frac{q_1}{Đ_1}+\frac{q_2}{Đ_2}} = \frac{x_1}{\frac{x_1}{Đ_1}+\frac{x_2}{Đ_2}}; \\
\Delta_{21} = \Delta_{22} &= \frac{c_2}{\frac{c_1}{Đ_1}+\frac{c_2}{Đ_2}} = \frac{q_2}{\frac{q_1}{Đ_1}+\frac{q_2}{Đ_2}} = \frac{x_2}{\frac{x_1}{Đ_1}+\frac{x_2}{Đ_2}}
\end{aligned} \qquad (39)$$

Detailed derivation of eq. (39) is provided in the Supporting Information accompanying our earlier publication [28]. It is noteworthy that in the *correlations dominant* scenario, described by eq. (39), the exchange coefficients do not appear. These equations imply that the elements Δ_{ij} can be calculated using the pure component $Đ_i$, without requiring information on the exchange coefficient $Đ_{12}$.

Figures 12a, and 12b show the MD simulated values of Δ_{ij} for $CH_4(1)$-$C_2H_6(2)$ mixtures, with c_1/c_2=25/75, in MFI as a function of the total pore concentration c_t. The calculations of the elements Δ_{ij} using the pure component $Đ_i$ values (open symbols) using eq. (39) are denoted by the continuous solid line. We note that eq. (39) provides a reasonably good quantitative prediction of the Δ_{ij} at values of c_t exceeding 15 kmol m^{-3}. The inflection in the Δ_{ij}, observed at a loading of 13 kmol m^{-3} is to be ascribed to the corresponding inflection in the pure component M-S diffusivity of C_2H_6.

Exactly analogous results are obtained for $C_2H_6(1)$-$C_3H_8(2)$ mixtures in MFI; see 12c, and 12d.

For both alkane mixtures considered in Figures 12 we note that the diagonal element of the tardier species, Δ_{22}, equals the calculations of the correlations dominant scenario over the entire composition range, and not just near saturation concentrations. This is a physically rational result. Correlations tend to slow down the more mobile species and in the limit of correlations being dominant, the calculations using eq. (39) tend to equal the value of the diffusivity of the tardier species.

For the special case of an equimolar binary mixture, i.e. c_1=c_2, eq. (39) further simplifies to yield

$$\Delta_{11} = \Delta_{12} = \Delta_{22} = \Delta_{21} = \frac{1}{\frac{1}{Đ_1} + \frac{1}{Đ_2}} \qquad (40)$$

This indicates that all four elements of the matrix [Δ] are equal to one another, and there is just one characteristic diffusivity in the mixture.

Figures 13, 14, 15, 16 present data on MD simulated values of Δ_{ij} for equimolar binary mixtures $CH_4(1)/C_2H_6(2)$, $CH_4(1)/C_3H_8(2)$, $CH_4(1)/CO_2(2)$, Ne(1)/Ar(2) in a variety of zeolites and MOFs, as a function of the total pore concentration c_t= c_1+c_2. As saturation is approached, all the Δ_{ij} appear to converge to the *same* value. The continuous lines are the predictions of eq. (40) using the pure component $Đ_1$, and $Đ_2$ from MD simulations. In all cases the Δ_{ij} are seen to converge towards one another, and eq. (40) is a reasonably good representation of Δ_{ij} of this limiting value.

In this context it is worth mentioning that for mixture diffusion in carbon nanotubes, MD simulations have shown that eq. (40) holds over the entire range of pore concentrations, and not just near saturation conditions [13, 41-43].

6. Comparing $Đ_1$ and $Đ_2$ for unary diffusion with those backed out from MD simulations for binary mixtures

The persuasive advantages for use of the M-S equations (30) in preference to the alternative Onsager or Fickian formulations is that in most cases the coefficients $Đ_1$, and $Đ_2$, that characterize species i – pore wall interactions in the broadest sense, can be identified with those determined for *unary* systems [13]. To illustrate this, Figure 17 provides data on the M-S diffusivity of CO_2, $Đ_i$, determined MD simulation data for diffusion of a variety of equimolar ($c_1 = c_2$) binary mixtures of CO_2 and different partner species in six different host materials (a) MFI, (b) FAU-Si, (c) IRMOF-1, (d) CuBTC, (e) MgMOF-74, and (f) CHA. Since correlations are of negligible importance for CHA, the presented data is for the self-diffusivities, $Đ_{i,self}$. For any host material, we note that the diffusivity of CO_2 in a binary mixture is practically independent of the partner species. Furthermore, when compared at the same total pore concentration of the adsorbed phase within the pores, $c_t = c_1 + c_2$, the values of $Đ_i$ are nearly the same in the mixture as those determined for *unary* diffusion, indicated by the red circles in Figure 17. Similar conclusions hold for the diffusivity of CH_4 in mixture containing different partner species; see Figure 18. These conclusions are of general validity for mixtures in which no cluster formation occurs; exceptional circumstances are discussed later.

7. Relating $Đ_{12}$ in *meso*-porous materials to fluid phase $Đ_{12,fl}$

In the absence of pore walls, i.e. in *fluid phase* mixtures, the molecule-molecule interactions are quantified by the M-S diffusivity $Đ_{12,fl}$. As illustration, Figure 19 presents MD simulation data on $Đ_{12,fl}$ for H_2/CH_4, CO_2/H_2, CH_4/CO_2, CH_4/Ar, CH_4/C_2H_6, and CH_4/C_3H_8 mixtures as a function of the total molar concentration c_t; these simulations were carried out with the methodology described in the literature [23]. MD simulations of $Đ_{12}$ in BTP-COF, that consists of one-dimensional (1D) hexagonal

shaped channels of 3.4 nm size are in excellent agreement with the values of $Đ_{12,fl}$ over the range of c_t. This conclusion also holds for cylindrical mesopores of 2 nm, 3 nm, 4 nm, and 5.8 nm. This leads us to conclude that the assumption that molecule-molecule interactions in mesoporous hosts is practically the same as that within the same *fluid phase* mixture at the same total molar concentration, c_t, i.e. $Đ_{12} = Đ_{12,fl}$.

Reliable procedures for estimation of $Đ_{12,fl}$ from molecular properties of the individual species are available in the literature, offering the possibility of *a priori* estimations of correlations. As illustration, the continuous solid lines in Figure 19 show the estimations of $Đ_{12,fl}$ using the method of Fuller, Schettler and Giddings (FSG) [26], developed for *ideal gas* mixtures. We note that for concentrations $c_t < 6$ kmol m^{-3}, the MD simulated $Đ_{12,fl}$ values are in excellent agreement with the FSG estimations. For concentrations $c_t > 6$ kmol m^{-3}, the $Đ_{12,fl}$ values reflect those in dense condensed fluids, for which some estimation procedures are also available in the literature [27].

8. Relating $Đ_{12}$ in *micro*-porous materials to fluid phase $Đ_{12,fl}$

For micro-porous materials, the exchange coefficient $Đ_{12}$ cannot be directly identified with the corresponding fluid phase diffusivity $Đ_{12,fl}$ because the molecule-molecule interactions are also significantly influenced by molecule-wall interactions. This is underscored by MD data for $Đ_{12}$ for six binary mixtures in a variety of micro-porous hosts; see Figure 20. For every guest/host combination, at any specific c_t, the $Đ_{12}$ is lower than the value of $Đ_{12,fl}$. The extent of lowering can be quantified by defining the fraction F

$$F \equiv Đ_{12} / Đ_{12,fl} \tag{41}$$

Every guest/host combination can be characterized by a constant fraction F, that is determined by data fitting. For "open" structures, with large pore volumes, V_p, the values of F are closer to unity. For example, for CH_4/Ar diffusion in IRMOF-1, COF-102, COF-103, and COF-108, the values are $F = 0.6$, 0.65, 0.65, and 0.8, respectively, increasing with increasing void fractions, ϕ. Remarkably, for IRMOF-1, the fraction F is in the narrow range of 0.6 – 0.7 for every guest mixture investigated.

At the other end of the spectrum, materials with low pore volumes, the values of the fraction F lie significantly below unity. In MFI that has a set of intersecting channels, F lies in the range of 0.1 – 0.15 for all mixtures. For BEA, also with intersecting channels, but with a slightly higher void fraction, we obtain F = 0.2. For materials such as FAU, NaX, NaY, LTA, and MgMOF-74 with intermediate void fractions, the values of F fall in range 0.3 – 0.6.

Figure 21 presents a plot of F as a function of the pore volume V_p of different porous host materials for nine different binary mixtures. The correlation is not perfect, suggesting that other aspects such as channel dimensions, and pore connectivity are also determinants of the exchange coefficient $Đ_{12}$.

The similarity in the plots for unary (Figure 6), and binary mixtures (Figure 21) is noteworthy.

9. Estimating $Đ_{12}$ from information on self-exchange coefficients $Đ_{ii}$

The Vignes interpolation formula (19), for binary fluid mixtures, can be extended to apply to porous materials in the following manner

$$Đ_{12} = \left(Đ_{11}\right)^{x_1}\left(Đ_{22}\right)^{x_2} \tag{42}$$

Equation (42) follows from Equation (19) since the binary and self-exchange coefficients share the same dependence on the structural parameters of relevance. Figure 22 provides a comparison of the predictions of the interpolation formula (42) with MD simulations of $Đ_{12}$ for six different guest/host combinations. Equation (42) is seen to be of good accuracy for all guest/host combinations.

Equation (32), in combination with Vignes interpolation formula (42) allows the estimate of Δ_{ij} from unary diffusivity data on $Đ_1$, $Đ_2$, $Đ_{11}$, and $Đ_{22}$. The applicability of this approach is demonstrated in Figure 23 for diffusion of an equimolar mixture of CH_4 (1) and CO_2 (2) in IRMOF-1. The MD simulated values (filled symbols) of (a) Δ_{11}, (b) Δ_{22}, and (c) Δ_{12} for an equimolar mixture of CH_4 (1) and CO_2 (2) in IRMOF-1 at 300 K are compared with the esimations of equation (32) along with the Vignes interpolation formula (42); these are shown by the solid black continuous lines. Similar good predictions are realized for an extremely wide variety of guest-host combinations.[16] We note from the data in Figure 23 that correlations have the effect of reducing *both* the diagonal Δ_{ii} below the pure

component $Đ_i$ values. The reduction is more severe for the more mobile CH_4. It is generally true that the more mobile the species, the more it is affected by correlations; this is because the tardier species do not vacate sites often enough.

Also shown are the predictions, using data determined for pure component MD simulations of $Đ_1$, and $Đ_2$, together with the negligible correlations scenario (equation (38), shown by the continuous solid red lines), and the correlations dominant scenario (equation (39), shown by the dashed blue lines). The MD simulated values (filled symbols) of (a) Δ_{11}, (b) Δ_{22}, and (c) Δ_{12} lie between these two limiting scenarios.

10. Influence of cluster formation due to hydrogen bonding

Exceptional circumstances prevail in cases of severe molecular segregation [13, 44] or cluster formation [17, 34, 36, 38]; in such situations, the coefficients $Đ_1$, and $Đ_2$ in the mixture are significantly different to those determined from unary experiments or simulations. For water/alcohol mixture diffusion, the diffusivity of each component is lowered due to molecular clusters being formed as a consequence of hydrogen bonding. This is illustrated in Figure 24 that present MD simulations of $Đ_1$, and $Đ_2$ for (a) water/methanol, (b) water/ethanol, and (c) methanol/ethanol mixture diffusion in FAU-Si zeolites. For (a) water/methanol, and (b) water/ethanol mixtures the diffusivity of water is reduced with increasing proportion of alcohol in the mixture. Hydrogen bonding between water and alcohol molecule pairs serves to act as a "flexible leash" linking the motion of the more mobile (water) and tardier (alcohol) species. The net result is that the motion of water is retarded due to cluster formation. Molecular clustering also has the effect of reducing the M-S diffusivity of the alcohol for low concentrations of water.

For methanol/ethanol mixture diffusion, the influence of molecular clustering is practically non-existent; the composition dependence of For MFI, the diffusivity of methanol is practically independent of composition, while that for $Đ_1$, and $Đ_2$ in the mixture are "normal"; Figure 24c.

MD data for water/alcohol mixture diffusion in MFI, CHA, and DDR provide additional evidence of the influence of molecular clustering; see our earlier work [33] for further details.

A wide variety of experimental data provide confirmation of the influence of molecular clustering on water/alcohol mixture diffusion in a variety of porous materials.

The NMR spectroscopy data of Hallberg et al.[45] on self-diffusivities in water-methanol mixtures across a Nafion membrane shows that the methanol diffusivity decreases significantly with increasing water composition.

For water/alcohol pervaporation across CHA zeolite membrane, the experimental data of Hasegawa et al. [46] show that the alcohol fluxes *decrease* with increasing water composition in the feed.. Indeed, *both* water and alcohol fluxes are reduced with increasing concentrations of partner species in the mixture. Similar experimental data for water/alcohol pervaporation across DDR membranes are reported [47].

For industrial scale water/NMP pervaporation across CHA membrane, the permeances of both components in the mixture are influenced, primarily reduced, due to cluster formation in the mixture [48].

The experimental data on pervaporation of water/ethanol mixtures across LTA-4A membrane [49], provides evidence of mutual-slowing down effects resulting from molecular clustering.

11. Intersection blocking and traffic-junction effects in MFI zeolite

Branched alkanes, benzene, alkyl benzenes, and cyclohexane prefer to locate at the channel intersections of MFI zeolite. The preferential location is because of molecular configuration effects; the intersections afford extra "leg room" [50]. A snapshot of the location of benzene is shown in Figure 25a as illustration. There are only 4 intersection sites available per unit cell of MFI. This implies that to obtain loadings higher than $\Theta_i = 4$ molecules per unit cell, an extra "push" will be required to locate the molecules elsewhere within the channels. Consequently, the pure component isotherms exhibit strong inflections at $\Theta_i = 4$ molecules per unit cell; see isotherms of iso-butane (iC4), benzene, 2-methylpentane (2MP), and 2,2dimethylbutane (22DMB) in Figure 25b.

Figure 26 showing the location of molecules in mixtures of n-butane(nC4)/iso-butane(iC4), n-hexane(nC6)/2,2dimethylbutane (22DMB), and ethene/benzene mixtures. The partner molecules nC4,

nC6, and ethene can located anywhere along the channels in the three mixtures, whereas the branched and cyclic hydrocarbons locate preferentially at the intersections of the channel structures of MFI zeolite [51]. There are important consequences for mixture diffusion, as we discuss below.

In the PFG NMR investigation of Fernandez et al.[52] the self-diffusivity in MFI of n-butane (nC4), in mixtures with iso-butane (iC4), was found to decreases to nearly zero as the loading of iC4 is increased from $\Theta_{iC4} = 0$ to 2 molecules per unit cell; see Figure 27a. The reason for this strong decline can be understood on the basis of the preferential location of iC4 at the channel intersections of MFI. For $\Theta_{iC4} = 2$, half the total number of intersections are occupied by iC4, that has a diffusivity which is about three orders of magnitude lower than that of nC4. Since the occupancy of the intersections is distributed randomly, each of the straight channels has an iC4 molecule ensconced somewhere along the channels; this is evident from the snapshot in Figure 26a. This is tantamount to blockage and leads to severe reduction in the molecular traffic of the intrinsically more mobile nC4. Uptake experiments of Chmelik et al.[53] provide further evidence of the influence iC4 has on co-diffusion of nC4 in MFI crystals.

PFG NMR studies of Förste et al.[54] found that the self-diffusivity of CH_4 in MFI is significantly reduced as the loading of the co-adsorbed benzene increases; see Figure 27b. The explanation is again to be found in the hindering of CH_4 diffusion due to blocking of the intersections by benzene [54].

For analogous reasons, the branched alkanes 2-methylpentane (2MP), causes the reduction in the self-diffusivity of the n-hexane (nC6) in nC6/ 2MP mixtures [55]; see Figure 27c.

When intersection blocking effects occur, the pure component diffusivities of the more mobile partner, that locates anywhere along the channels of MFI, cannot be identified with those in the mixture.

12. Conclusions

The major conclusions of the present study are summarized below.

(1) The factoring-out of the thermodynamic correction factor often leads to simpler physical interpretation of the diffusivities in nanoporous crystalline materials

(2) When no cluster formation occurs, the M-S diffusivities of constituent species in a binary mixture, $Đ_1$, and $Đ_2$ are practically the same as that for unary diffusion, when determined at the total pore concentration in the mixture, c_t. This implies that the experimental data on unary permeation across membranes, say, can be used to predict the corresponding values for mixture permeation.

(3) For mixture diffusion inside cylindrical silica meso-pores, $d_p > 2$ nm, the binary exchange coefficient $Đ_{12}$, is found to be equal to the corresponding value in the binary fluid mixture, $Đ_{12,fl}$, over the entire range of mixture concentrations, c_t. For porous structures such as COF-102, COF-103, and COF-108 with large voidages and pore volumes, $F \approx 1$.

(4) For each guest/host combination, over the entire range of pore concentrations, it was found that $Đ_{12}$ is a constant fraction, F, of the M-S diffusivity in the fluid phase, $Đ_{12,fl}$, when compared at the same value of pore concentration, c_t. The fraction, F, is primarily dependent on the host material, and has values in the range of 0.1 – 1. For intersecting channels structures of MFI, with channels of 5.5 Å, the value of F is in the narrow range of 0.1 – 0.15. For structures such as FAU, MgMOF-74, and IRMOF-1 the values of F fall in range of 0.4 – 0.7.

(5) Analogously, the self-exchange coefficient for unary diffusion $Đ_{ii}$ inside micro-porous structures is related to the fluid phase self-diffusivity $Đ_{ii,fl}$ by a constant factor F.

(6) The degree of correlations effects, as quantified by the ratio $Đ_1/Đ_{12}$, are *stronger* in open structures with larger pore volumes, and in 1D channels. Correlations are relatively insignificant in cage-type structures in which adjacent cages are separated by narrow windows.

(7) For mixtures in which cluster formation occurs, say due to hydrogen bonding, $Đ_1$, and $Đ_2$ in the mixture cannot be identified with the unary values. Due to cluster formation, the Maxwell-Stefan diffusivity, $Đ_i$, of either component in water-alcohol mixtures is lowered below the corresponding values of the pure components. In practice we need to take account of the influence of mixture composition on the $Đ_i$.

(8) Within the intersecting channels of MFI zeolite, branched and cyclic hydrocarbons locate preferentially at the intersections. This causes intersection blocking of more mobile partners that locate within the channels. The M-S diffusivity of the more mobile partner cannot be identified with the pure component values. Intersection blocking effects cannot be modeled adequately within the framework of the M-S theory.

13. Notation

b_A	dual-Langmuir-Freundlich constant for species *i* at adsorption site A, $Pa^{-\nu_i}$
b_B	dual-Langmuir-Freundlich constant for species *i* at adsorption site B, $Pa^{-\nu_i}$
[*B*]	matrix of inverse M-S coefficients, defined by eq. (8), m^{-2} s
c_i	pore concentration of species *i*, mol m^{-3}
c_t	total pore concentration in mixture, mol m^{-3}
d_p	pore diameter, m
D_i	Fick diffusivity of species *i*, m^2 s^{-1}
$Đ_i$	M-S diffusivity of species *i*, m^2 s^{-1}
$Đ_{ii}$	self-exchange coefficient, m^2 s^{-1}
$Đ_{ii,fl}$	self-diffusivity of species *i* in fluid phase, m^2 s^{-1}
$Đ_{12}$	M-S exchange coefficient, m^2 s^{-1}
$Đ_{12,fl}$	M-S diffusivity in binary fluid mixture, m^2 s^{-1}
$D_{i,self}$	self-diffusivity of species *i*, m^2 s^{-1}
f_i	partial fugacity of species *i*, Pa
f_t	total fugacity of bulk fluid mixture, Pa
F	factor defined by equation (41), dimensionless
n	number of species in the mixture, dimensionless
N_i	molar flux of species *i* defined in terms of the cross-sectional area of the crystalline framework, mol m^{-2} s^{-1}
R	gas constant, 8.314 J mol^{-1} K^{-1}
T	absolute temperature, K
V_p	accessible pore volume, m^3 kg^{-1}
x_i	mole fraction of species *i* based on loading within pore, dimensionless

Greek letters

δ_{ij}	Kronecker delta, dimensionless
[Δ]	matrix defined of M-S diffusivities, m^2 s^{-1}

Δ_{ij}	elements of $[\Delta]$, $m^2\ s^{-1}$
γ_i	activity coefficient of component *i* in adsorbed phase, dimensionless
Γ_{ij}	thermodynamic factors, dimensionless
$[\Gamma]$	matrix of thermodynamic factors, dimensionless
ϕ	fractional pore volume of microporous material, dimensionless
θ_i	fractional occupancy of component *i*, dimensionless
θ_V	fractional vacancy, dimensionless
Θ_i	loading of species *i*, molecules per unit cell
$\Theta_{i,sat}$	saturation loading of species *i*, molecules per unit cell
Θ_t	total molar loading of mixture, molecules per unit cell
ρ	framework density, $kg\ m^{-3}$

Subscripts

fl	referring to site fluid phase
i	referring to component *i*
fl	referring to fluid phase
t	referring to total mixture

Table 1. Salient structural information on zeolites.

Structure	Topology	Fractional pore volume, ϕ	Pore volume/ cm^3/g	Framework density/ kg/m^3
AFI	12-ring 1D channels of 7.3 Å size	0.274	0.159	1730
BEA	Intersecting channels of two sizes: 12-ring of 6.1 Å - 6.8 Å and 10-ring of 5.6 Å – 6.7 Å	0.408	0.271	1509
BOG	Intersecting channels: 12-ring 6.8 Å -7.4 Å and 10-ring of 5.6 Å - 5.8 Å	0.374	0.241	1996
CHA	316 $Å^3$ cages separated by 3.77 Å × 4.23 Å size windows	0.382	0.264	1444
DDR	277.8 $Å^3$ cages separated by 3.65 Å × 4.37 Å size windows	0.245	0.139	1760
ERI	408 $Å^3$ cages separated by 3.8 Å – 4.9 Å size windows	0.363	0.228	1595
FAU-Si	790 $Å^3$ cages separated by 7.4 Å size windows	0.439	0.328	1338
FER	10-ring 1D main channels of 4.2 Å -5.4 Å size, connected with 8-ring side pockets of 3.5 Å -4.8 Å size	0.283	0.160	1772
ISV	Intersecting channels of two sizes: 12-ring of 6.1 Å -6.5 Å and 12-ring of 5.9 Å - 6.6 Å	0.426	0.278	1533
ITQ-29	678 $Å^3$ cages separated by 4 Å × 4.22 Å size windows	0.405	0.283	1433
LTL	12-ring 1D channels of 7.1 Å size	0.277	0.170	1627
LTA-Si	743 $Å^3$ cages separated by 4.11 Å × 4.47 Å size windows	0.399	0.310	1285
LTA-4A	694 $Å^3$ cages separated by 4 Å × 4.58 Å size windows	0.38	0.25	1530
LTA-5A	702 $Å^3$ cages separated by 4 Å × 4.58 Å size windows	0.38	0.25	1508
MFI	10-ring intersecting channels of 5.4 Å – 5.5 Å and 5.4 Å – 5.6 Å size	0.297	0.165	1796
MOR	12-ring 1D main channels of 6.5 Å -7 Å size, connected with 8-ring side pockets of 2.6 Å -5.7 Å size	0.285	0.166	1715
MTW	12-ring 1D channels of 5.6 Å -6 Å size	0.215	0.111	1935
NaY	790 $Å^3$ cages separated by 7.4 Å size windows	0.41	0.303	1347
NaX	790 $Å^3$ cages separated by 7.4 Å size windows	0.40	0.280	1421
TON	10-ring 1D channels of 4.6 Å -5.7 Å size	0.190	0.097	1969

Table 2. Salient structural information on MOFs, ZIFs, and COFs.

Structure	Topology	Fractional pore volume, ϕ	Pore volume/ cm^3/g	Framework density/ kg/m^3
CuBTC	Large cages are inter-connected by 9 Å windows of square cross-section. The large cages are also connected to tetrahedral-shaped pockets of ca. 6 Å size through triangular-shaped windows of 4.6 Å size	0.759	0.863	879
IRMOF-1	Two alternating, inter-connected, cavities of 10.9 Å and 14.3 Å with window size of 8 Å.	0.812	1.369	593
Zn(bdc)dabco	There exist two types of intersecting channels of about 7.5 Å × 7.5 Å along the x-axis and channels of 3.8 Å × 4.7 Å along y and z axes.	0.662	0.801	826
Co(bdc)dabco	There exist two types of intersecting channels of about 7.6 Å × 7.6 Å along the x-axis and channels of 3.7 Å × 5.1 Å along y and z axes.	0.648	0.796	814
MOF-177	Six diamond-shaped channels (upper) with diameter of 10.8 Å surround a pore containing eclipsed BTB^{3-} moieties.	0.840	1.968	427
Co(BDP)	1D square-shaped channels of 10 Å	0.67	0.927	721
MgMOF-74	1D hexagonal-shaped channels of 11 Å	0.708	0.782	905
NiMOF-74	1D hexagonal-shaped channels of 11 Å	0.695	0.582	1193
CoMOF-74	1D hexagonal-shaped channels of 11 Å	0.707	0.599	1180
ZnMOF-74	1D hexagonal-shaped channels of 11 Å	0.709	0.582	1219
FeMOF-74	1D hexagonal-shaped channels of 11 Å	0.705	0.626	1126
MIL-47	1D diamond-shaped channels of 8.5 Å	0.608	0.606	1004
MIL-53 (Cr)-lp	1D lozenge-shaped channels of 8.5 Å	0.539	0.518	1041
BTP-COF	1D hexagonal-shaped channels of 34 Å	0.752	1.79	420
COF-102	Cavity of size 8.9 Å	0.8	1.875	426
COF-103	Cavity of size 9.6 Å	0.82	2.040	400
COF-108	Two cavities, of sizes 15.2 Å and 29.6 Å	0.93	5.467	170
ZIF-7		0.277	0.223	1241
ZIF-8	1168 $Å^3$ cages separated by 3.26 Å size windows	0.476	0.515	924

14. References

[1] J. Kärger, D.M. Ruthven, D.N. Theodorou, Diffusion in Nanoporous Materials, Wiley - VCH, Weinheim, 2012.

[2] J. Caro, Are MOF membranes better in gas separation than those made of zeolites?, Curr. Opin. Chem. Eng. 1 (2011) 77-83.

[3] J. Gascon, F. Kapteijn, Metal-Organic Framework Membranes—High Potential, Bright Future?, Angew. Chem. Int. Ed. 49 (2010) 1530-1532.

[4] R. Krishna, J.M. van Baten, In Silico Screening of Zeolite Membranes for CO_2 Capture, J. Membr. Sci. 360 (2010) 323-333.

[5] R. Krishna, J.M. van Baten, In silico screening of metal-organic frameworks in separation applications, Phys. Chem. Chem. Phys. 13 (2011) 10593-10616.

[6] R. Krishna, J.R. Long, Screening metal-organic frameworks by analysis of transient breakthrough of gas mixtures in a fixed bed adsorber, J. Phys. Chem. C 115 (2011) 12941-12950.

[7] Y. He, R. Krishna, B. Chen, Metal-Organic Frameworks with Potential for Energy-Efficient Adsorptive Separation of Light Hydrocarbons, Energy Environ. Sci. 5 (2012) 9107-9120.

[8] D. Dubbeldam, R. Krishna, S. Calero, A.Ö. Yazaydın, Computer-Assisted Screening of Ordered Crystalline Nanoporous Adsorbents for Separation of Alkane Isomers, Angew. Chem. Int. Ed. 51 (2012) 11867-11871.

[9] A.I. Skoulidas, D.S. Sholl, R. Krishna, Correlation effects in diffusion of CH_4/CF_4 mixtures in MFI zeolite. A study linking MD simulations with the Maxwell-Stefan formulation, Langmuir 19 (2003) 7977-7988.

[10] S. Chempath, R. Krishna, R.Q. Snurr, Nonequilibrium MD simulations of difusion of binary mixtures containing short n-alkanes in faujasite, J. Phys. Chem. B 108 (2004) 13481-13491.

[11] R. Krishna, Describing the diffusion of guest molecules inside porous structures, J. Phys. Chem. C 113 (2009) 19756-19781.

[12] R. Krishna, Diffusion in Porous Crystalline Materials, Chem. Soc. Rev. 41 (2012) 3099-3118.

[13] R. Krishna, J.M. van Baten, Onsager coefficients for binary mixture diffusion in nanopores, Chem. Eng. Sci. 63 (2008) 3120-3140.

[14] N. Hansen, F.J. Keil, Multiscale modeling of reaction and diffusion in zeolites: from the molecular level to the reactor, Soft Mater. 10 (2012) 179-201.

[15] R. Krishna, J.M. van Baten, An investigation of the characteristics of Maxwell-Stefan diffusivities of binary mixtures in silica nanopores, Chem. Eng. Sci. 64 (2009) 870-882.

[16] R. Krishna, J.M. van Baten, Unified Maxwell-Stefan description of binary mixture diffusion in micro- and meso- porous materials, Chem. Eng. Sci. 64 (2009) 3159-3178.

[17] R. Krishna, J.M. van Baten, Hydrogen bonding effects in adsorption of water-alcohol mixtures in zeolites and the consequences for the characteristics of the Maxwell-Stefan diffusivities, Langmuir 26 (2010) 10854-10867.

[18] R. Krishna, J.M. van Baten, Influence of Adsorption Thermodynamics on Guest Diffusivities in Nanoporous Crystalline Materials, Phys. Chem. Chem. Phys. 15 (2013) 7994-8016.

[19] R. Krishna, J.A. Wesselingh, The Maxwell-Stefan approach to mass transfer, Chem. Eng. Sci. 52 (1997) 861-911.

[20] W.M. Clark, R.L. Rowley, The mutual diffusion coefficient of methanol - n-hexane near the consolute point, A.I.Ch.E.J. 32 (1986) 1125-1131.

[21] R. Krishna, J.M. van Baten, MD simulations of diffusivities in methanol – n-hexane mixtures near the liquid-liquid phase splitting region, Chem Eng Technol 29 (2006) 516-519.

[22] A. Vignes, Diffusion in binary solutions, Ind. Eng. Chem. Fundamentals 5 (1966) 189-199.

[23] R. Krishna, J.M. van Baten, The Darken relation for multicomponent diffusion in liquid mixtures of linear alkanes. An investigation using Molecular Dynamics (MD) simulations, Ind. Eng. Chem. Res. 44 (2005) 6939-6947.

[24] R. Taylor, R. Krishna, Multicomponent mass transfer, John Wiley, New York, 1993.
[25] J.A. Wesselingh, R. Krishna, Mass transfer in multicomponent mixtures, Delft University Press, Delft, 2000.
[26] E.N. Fuller, P.D. Schettler, J.C. Giddings, A new method for prediction of binary gas-phase diffusion coefficients, Ind. Eng. Chem. 58 (1966) 19-27.
[27] B.E. Poling, J.M. Prausnitz, J.P. O'Connell, The Properties of Gases and Liquids, McGraw-Hill, 5th Edition, New York, 2001.
[28] R. Krishna, J.M. van Baten, Describing Mixture Diffusion in Microporous Materials under Conditions of Pore Saturation, J. Phys. Chem. C 114 (2010) 11557-11563.
[29] R. Krishna, J.M. van Baten, Letter to the Editor, A.I.Ch.E.J. 56 (2010) 3288-3289.
[30] R. Krishna, J.M. van Baten, Investigating the validity of the Knudsen prescription for diffusivities in a mesoporous covalent organic framework, Ind. Eng. Chem. Res. 50 (2011) 7083-7087.
[31] R. Krishna, J.M. van Baten, Investigating the validity of the Bosanquet formula for estimation of diffusivities in mesopores, Chem. Eng. Sci. 69 (2012) 684-688.
[32] W.G. Pollard, R.D. Present, On gaseous self-diffusion in long capillary tubes, Phys. Rev. 73 (1948) 762-774.
[33] R. Krishna, J.M. van Baten, Investigating the Influence of Diffusional Coupling on Mixture Permeation across Porous Membranes J. Membr. Sci. 430 (2013) 113-128.
[34] R. Krishna, J.M. van Baten, Investigating cluster formation in adsorption of CO_2, CH_4, and Ar in zeolites and metal organic frameworks at sub-critical temperatures, Langmuir 26 (2010) 3981-3992.
[35] C. Chmelik, J. Kärger, M. Wiebcke, J. Caro, J.M. van Baten, R. Krishna, Adsorption and diffusion of alkanes in CuBTC crystals investigated using infrared microscopy and molecular simulations, Microporous Mesoporous Mater. 117 (2009) 22-32.
[36] R. Krishna, J.M. van Baten, Highlighting a variety of unusual characteristics of adsorption and diffusion in microporous materials induced by clustering of guest molecules, Langmuir 26 (2010) 8450-8463.
[37] R. Krishna, J.M. van Baten, Highlighting Pitfalls in the Maxwell-Stefan Modeling of Water-Alcohol Mixture Permeation across Pervaporation Membranes, J. Membr. Sci. 360 (2010) 476-482.
[38] R. Krishna, J.M. van Baten, Mutual slowing-down effects in mixture diffusion in zeolites, J. Phys. Chem. C 114 (2010) 13154-13156.
[39] R. Krishna, J.M. van Baten, A molecular dynamics investigation of the unusual concentration dependencies of Fick diffusivities in silica mesopores, Microporous Mesoporous Mater. 138 (2011) 228-234.
[40] R. Krishna, J.M. van Baten, A rationalization of the Type IV loading dependence in the Kärger-Pfeifer classification of self-diffusivities, Microporous Mesoporous Mater. 142 (2011) 745-748.
[41] R. Krishna, J.M. van Baten, Describing binary mixture diffusion in carbon nanotubes with the Maxwell-Stefan equations. An investigation using molecular dynamics simulations, Ind. Eng. Chem. Res. 45 (2006) 2084-2093.
[42] H.B. Chen, D.S. Sholl, Rapid diffusion of CH_4/H_2 mixtures in single-wall carbon nanotubes, J. Amer. Chem. Soc. 126 (2004) 7778-7779.
[43] G. Arora, S.I. Sandler, Air separation by single wall carbon nanotubes: Mass transport and kinetic selectivity, J. Chem. Phys. 124 (2006) 084702.
[44] R. Krishna, J.M. van Baten, Segregation effects in adsorption of CO_2 containing mixtures and their consequences for separation selectivities in cage-type zeolites, Sep. Purif. Technol. 61 (2008) 414-423.
[45] F. Hallberg, T. Vernersson, E.T. Pettersson, S.V. Dvinskikh, G. Lindbergh, I. Furó, Electrokinetic transport of water and methanol in Nafion membranes as observed by NMR spectroscopy, Electrochim. Acta 55 (2010) 3542-3549.

[46] Y. Hasegawa, C. Abe, M. Nishioka, K. Sato, T. Nagase, T. Hanaoka, Formation of high flux CHA-type zeolite membranes and their application to the dehydration of alcohol solutions, J. Membr. Sci. 364 (2010) 318-324.
[47] J. Kuhn, J.M. Castillo-Sanchez, J. Gascon, S. Calero, D. Dubbeldam, T.J.H. Vlugt, F. Kapteijn, J. Gross, Adsorption and Diffusion of Water, Methanol, and Ethanol in All-Silica DD3R: Experiments and Simulation, J. Phys. Chem. C 113 (2009) 14290-14301.
[48] K. Sato, K. Sugimoto, N. Shimosuma, T. Kikuchi, T. Kyotani, T. Kurata, Development of practically available up-scaled high-silica CHA-type zeolite membranes for industrial purpose in dehydration of N-methyl pyrrolidone solution, J. Membr. Sci. 409-410 (2012) 82-95.
[49] M. Pera-Titus, C. Fité, V. Sebastián, E. Lorente, J. Llorens, F. Cunill, Modeling Pervaporation of Ethanol/Water Mixtures within 'Real' Zeolite NaA Membranes, Ind. Eng. Chem. Res. 47 (2008) 3213-3224.
[50] A. Gupta, L.A. Clark, R.Q. Snurr, Grand canonical Monte Carlo simulations of nonrigid molecules: Siting and segregation in silicalite zeolite, Langmuir 16 (2000) 3910-3919.
[51] R. Krishna, J.M. van Baten, Diffusion of hydrocarbon mixtures in MFI zeolite: Influence of intersection blocking, Chem. Eng. J. 140 (2008) 614-620.
[52] M. Fernandez, J. Kärger, D. Freude, A. Pampel, J.M. van Baten, R. Krishna, Mixture diffusion in zeolites studied by MAS PFG NMR and molecular simulation, Microporous Mesoporous Mater. 105 (2007) 124-131.
[53] C. Chmelik, L. Heinke, J.M. van Baten, R. Krishna, Diffusion of *n*-butane/*iso*-butane mixtures in silicalite-1 investigated using infrared (IR) microscopy, Microporous Mesoporous Mater. 125 (2009) 11-16.
[54] C. Förste, A. Germanus, J. Kärger, H. Pfeifer, J. Caro, W. Pilz, A. Zikánóvá, Molecular mobility of methane adsorbed in ZSM-5 containing co-adsorbed benzene, and the location of benzene molecules, J. Chem. Soc., Faraday Trans. 1. 83 (1987) 2301-2309.
[55] A.O. Koriabkina, A.M. de Jong, D. Schuring, J. van Grondelle, R.A. van Santen, Influence of the acid sites on the intracrystalline diffusion of hexanes and their mixtures within MFI-zeolites, J. Phys. Chem. B 106 (2002) 9559-9566.
[56] R. Krishna, Adsorptive separation of $CO_2/CH_4/CO$ gas mixtures at high pressures, Microporous Mesoporous Mater. 156 (2012) 217-223.
[57] R. Krishna, J.M. van Baten, Diffusion of alkane mixtures in zeolites. Validating the Maxwell-Stefan formulation using MD simulations, J. Phys. Chem. B 109 (2005) 6386-6396.
[58] R. Krishna, J.M. van Baten, Diffusion of alkane mixtures in MFI zeolite, Microporous Mesoporous Mater. 107 (2008) 296-298.
[59] R. Krishna, J.M. van Baten, Insights into diffusion of gases in zeolites gained from molecular dynamics simulations, Microporous Mesoporous Mater. 109 (2008) 91-108.
[60] R. Krishna, J.M. van Baten, Investigating the Relative Influences of Molecular Dimensions and Binding Energies on Diffusivities of Guest Species Inside Nanoporous Crystalline Materials J. Phys. Chem. C 116 (2012) 23556-23568.
[61] R. Krishna, J.M. van Baten, Investigating the potential of MgMOF-74 membranes for CO_2 capture, J. Membr. Sci. 377 (2011) 249-260.
[62] R. Krishna, J.M. van Baten, Maxwell-Stefan modeling of slowing-down effects in mixed gas permeation across porous membranes, J. Membr. Sci. 383 (2011) 289-300.
[63] C. Chmelik, H. Bux, J. Caro, L. Heinke, F. Hibbe, T. Titze, J. Kärger, Mass transfer in a nanoscale material enhanced by an opposing flux, Phys. Rev. Lett. 104 (2010) 085902.
[64] D. Schuring, A.O. Koriabkina, A.M. de Jong, B. Smit, R.A. van Santen, Adsorption and diffusion of n-hexane/2-methylpentane mixtures in zeolite silicalite: Experiments and modeling, J. Phys. Chem. B 105 (2001) 7690-7698.

15. Captions for Figures

Figure 1. Comparison of surface area, pore volumes, framework densities, fractional pore volumes, and characteristic dimensions of some representative zeolites, MOFs and ZIFs.

Figure 2. (a) Experimental data of Clark and Rowley [20] for the Fick diffusivities, $D_{12,fl}$, and Maxwell-Stefan diffusivities, $Đ_{12,fl}$,, for methanol – *n*-hexane mixtures at 313.15 K (b) Comparison of the experimental data of Clark and Rowley [20] with the MD simulations of Krishna and van Baten [21]. Also shown are the calculations using the Vignes interpolation formula (19).

Figure 3. MD simulations of self-diffusivities, $Đ_{ii,fl}$, along with the $Đ_{12,fl}$ for diffusion in a variety of equimolar binary fluid mixtures as a function of the total fluids concentration, c_t. The calculations of $Đ_{12,fl}$ following the Vignes interpolation formula (19) are shown by the continuous solid lines. The calculation of $Đ_{12,fl}$ using correlation of Fuller, Schettler and Giddings (FSG) [26], developed for *binary* gas mixtures, is indicated by the dashed lines. The MD data are culled from our previous publications [12, 13, 16, 30, 31, 56-62].

Figure 4. MD simulations of $D_{i,self}$, $Đ_i$, $Đ_{ii}$, and D_i, for CH_4 in (a) MFI, (b) NaX, (c) LTA-5A, (d) MgMOF-74, (e) IRMOF-1, and (f) BTP-COF, as a function of the pore concentrations c_i. Also indicated by open square symbols are the values of the fluid phase self-diffusivities, $Đ_{ii,fl}$, determined from MD simulations using the same force field parameters. Note that the data for LTA-5A is at 500 K, whereas the rest of the data are for 300 K.

Figure 5. The self-exchange coefficients $Đ_{ii}$, for unary diffusion of (a) CO_2, (b) CH_4, (c) H_2, (d) N_2, (e) Ar, and (f) Ne at 300 K in a variety of host materials as a function of the pore concentration, c_i. The $Đ_{ii,fl}$ for self-diffusivity in the *fluid phase*, obtained from independent MD simulations, are also presented in square symbols, along with continuous solid lines that represent the fraction F times $Đ_{ii,fl}$. The MD data are culled from our previous publications [12, 13, 16, 30, 31, 56-62].

Figure 6. Fraction F determined from MD simulations of the self-exchange coefficient for unary diffusion , expressed as a function of the pore volume of the micro-porous host structures, V_p.

Figure 7. (a) CBMC simulations of pure component isotherms for methanol and ethanol in ZIF-8 at 300 K [12, 17]. Also shown are the fits using equation (29). (b) The inverse thermodynamic factor, $1/\Gamma_i$, for methanol and ethanol adsorption in ZIF-8, obtained from analytic differentiation of the dual-Langmuir-Freundlich fits [12, 17].

Figure 8. Loading dependence of $Đ_i$, D_i, and $D_{i,self}$ for (a) methanol, and (b) ethanol in ZIF-8 [12, 17, 63].

Figure 9. Loading dependence of the Fick diffusivity D_i, and the thermodynamic factor Γ_i, for (a) neopentane (neo-P, T_c = 434 K) and (a) 2-methylbutane (2MB, T_c = 460 K) in CuBTC at 298 K. The symbols represent D_i, values determined from the IRM experiments of Chmelik et al.[35]. The continuous solid lines are derived from analytic differentiation of the isotherm fits.

Figure 10. MD simulated values of Δ_{ij} for equimolar binary $CO_2(1)/H_2(2)$ mixtures (c_1=c_2) in a variety of zeolites and MOFs, as a function of the total pore concentration c_t= c_1+c_2.

Figure 11. MD simulation data for the degree of correlations, $Đ_1/Đ_{12}$, for diffusion of equimolar binary mixtures (c_1 = c_2) (a) H_2/ CO_2, (b) CO_2/CH_4, (c) H_2/CH_4, (d) CH_4/nC_4H_{10}, (e) CH_4/C_2H_6, and (f) CH_4/C_3H_8 at 300 K in a variety of host materials, as a function of the total pore concentration, $c_t = (q_1 + q_2)/V_p$. As explained in previous works, the comparisons of diffusivities in different host materials is best done in terms of pore concentrations, expressed in terms of the accessible pore volume V_p [16].

Figure 12. MD simulated values (filled symbols) of Δ_{ij} for binary mixtures (a, b) $CH_4(1)$-$C_2H_6(2)$ and (c, d) $C_2H_6(1)$-$C_3H_8(2)$ in MFI at 300 K, as a function of the total pore concentration c_t= c_1+c_2. Also shown with open symbols are MD simulated pure component $Đ_1$, and $Đ_2$. The pore concentration ratio, c_1/c_2=25/75. The continuous lines are the predictions of equation (39) using the pure component $Đ_1$, and $Đ_2$ from MD simulations.

Figure 13. MD simulated values of Δ_{ij} for equimolar binary $CH_4(1)/C_2H_6(2)$ mixtures (c_1=c_2) in a variety of zeolites and MOFs, as a function of the total pore concentration c_t= c_1+c_2. The continuous lines are the predictions of equation (40) using the pure component $Đ_1$, and $Đ_2$ from MD simulations.

Figure 14. MD simulated values of Δ_{ij} for equimolar binary $CH_4(1)/C_3H_8(2)$ mixtures (c_1=c_2) in a variety of zeolites and MOFs, as a function of the total pore concentration c_t= c_1+c_2. The continuous lines are the predictions of equation (40) using the pure component $Đ_1$, and $Đ_2$ from MD simulations.

Figure 15. MD simulated values of Δ_{ij} for equimolar binary $CH_4(1)/CO_2(2)$ mixtures (c_1=c_2) in a variety of zeolites and MOFs, as a function of the total pore concentration c_t= c_1+c_2. The continuous lines are the predictions of equation (40) using the pure component $Đ_1$, and $Đ_2$ from MD simulations.

Figure 16. MD simulated values of Δ_{ij} for equimolar binary Ne(1)/Ar(2) mixtures (c_1=c_2) in a variety of zeolites and MOFs, as a function of the total pore concentration c_t= c_1+c_2. The continuous lines are the predictions of equation (40) using the pure component $Đ_1$, and $Đ_2$ from MD simulations.

Figure 17. Maxwell-Stefan diffusivity of CO_2, $Đ_i$, determined MD simulation data for diffusion of a variety of equimolar ($c_1 = c_2$) binary mixtures of CO_2 and different partner species in (a) MFI, (b) FAU-Si, (c) IRMOF-1, (d) CuBTC, (e) MgMOF-74, and (f) CHA. The *x*- axis represent the total pore concentration of the adsorbed phase within the pores, $c_t = c_1 + c_2$. Also shown in red circles are the MD simulations of $Đ_i$, for unary diffusion. For CHA, the plotted diffusivities are the self-diffusivities, $D_{i,self}$, that are more accurate to determine for CHA and provide good approximations of the M-S diffusivities, i.e. $D_{i,self} \approx Đ_i$. The MD data are culled from our previous publications [12, 13, 16, 56-62].

Figure 18. Maxwell-Stefan diffusivity of CH_4, $Đ_i$, determined MD simulation data for diffusion of a variety of equimolar ($c_1 = c_2$) binary mixtures of CH_4 and different partner species in (a) MFI, (b) FAU-Si, (c) IRMOF-1, (d) CuBTC, (e) MgMOF-74, and (f) CHA. The x- axis represent the total pore concentration of the adsorbed phase within the pores, $c_t = c_1 + c_2$. Also shown in green squares are the MD simulations of $Đ_i$, for unary diffusion. For CHA, the plotted diffusivities are the self-diffusivities, $D_{i,self}$, that are more accurate to determine for CHA and provide good approximations of the M-S diffusivities, i.e. $D_{i,self} \approx Đ_i$. The MD data are culled from our previous publications [12, 13, 16, 56-62].

Figure 19. The MD simulations for fluid phase diffusivity $Đ_{12,fl}$ (square symbols) for equimolar ($c_1 = c_2$) (a) H_2/CH_4, (b) CO_2/H_2, (c) CH_4/CO_2, (d) CH_4/Ar, (e) CH_4/C_2H_6, and (f) CH_4/C_3H_8 mixtures as a function of the total fluid phase molar concentration c_t. The calculation of $Đ_{12,fl}$ using correlation of Fuller, Schettler and Giddings (FSG) [26], developed for *binary* gas mixtures, is indicated by the continuous solid line. Also indicated are MD data for the exchange coefficients $Đ_{12}$ in cylindrical silica mesopores (of diameters 3 nm, 4 nm, and 5.8 nm), and BTP-COF (with 3.4 nm size 1D hexagonal-shaped channels). The MD data are culled from our previous publications [12, 13, 16, 30, 31, 56-62].

Figure 20. The M-S binary exchange coefficients $Đ_{12}$, for diffusion of equimolar ($c_1 = c_2$) binary mixtures (a) H_2/CH_4, (b) CH_4/Ar, (c) CH_4/C_2H_6, (d) CH_4/CO_2, (e) H_2/CO_2, and (f) CO_2/N_2 at 300 K in a variety of host materials as a function of the total pore concentration, c_t. The $Đ_{12,fl}$ for binary *fluid phase* mixture diffusion, obtained from independent MD simulations, are also presented in square symbols, along with continuous solid lines that represent the fraction F times $Đ_{12,fl}$. The MD data are culled from our previous publications [12, 13, 16, 30, 31, 56-62].

Figure 21. Fraction F determined from MD simulations of the exchange coefficient for binary mixtures, expressed as a function of the pore volume of the micro-porous host structures, V_p.

Figure 22. Test of the Vignes interpolation formula (42) for diffusion in a variety of binary mixtures in different microporous hosts. The MD data are culled from our previous publications [12, 13, 16, 30, 31, 56-62].

Figure 23. MD simulated values (filled symbols) of (a) Δ_{11}, (b) Δ_{22}, and (c) Δ_{12} for an equimolar mixture of CH_4 (1) and CO_2 (2) in IRMOF-1 at 300 K. The continuous lines are the predictions of equation (32) along with the Vignes interpolation formula (42). Also shown are the predictions, using data determined for pure component MD simulations of $Đ_1$, and $Đ_2$, together with the negligible correlations scenario (equation (38)), and the correlations dominant scenario (equation (39)).

Figure 24. Maxwell-Stefan diffusivities, $Đ_i$, in (a) water/methanol, (b) water/ethanol, and (c) methanol/ethanol mixtures of varying composition in FAU-Si; the data are compiled from MD simulation results published in the literature [17, 37, 38].

Figure 25. (a) Snapshot showing the location of benzene molecules at the intersections of MFI. (b) CBMC simulations of the pure component isotherms for iC4, 2MP, 22DMB, benzene and nC7 in MFI at 300 K.

Figure 26. Snapshots showing the location of molecules of (a) nC4/iC4, (b) nC6/22DMB, and (c) ethene/benzene mixtures in MFI.

Figure 27. (a) PFG NMR experimental data [52] on self-diffusion coefficients of nC4 in nC4/iC4 mixtures in MFI as a function of the loading of iC4 in the mixture. (b) PFG NMR experimental data [54] on self-diffusion coefficients of CH_4 in CH_4/Benzene mixtures in MFI as a function of the loading of Benzene in the mixture. (c) Experimental data [64] on self-diffusivities of nC6 and 2methylpentane (2MP) as a function of the loading of 2MP in MFI zeolite

Figure 1

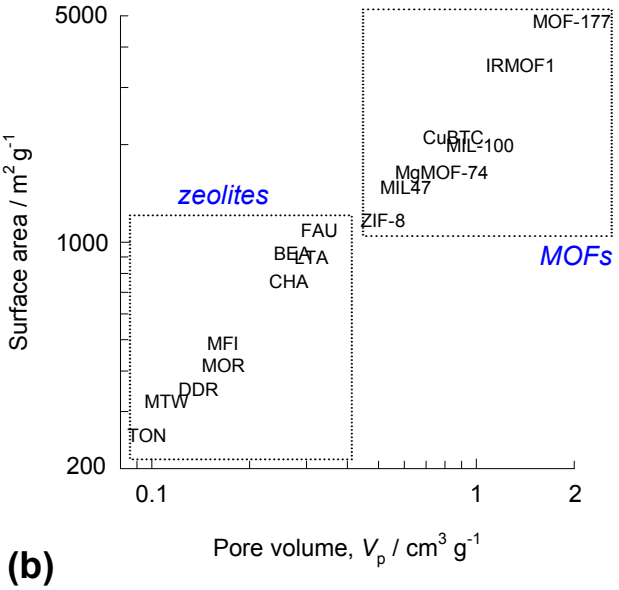
(a)
5000
1000
200
0.1
1
2
Surface area / m^2 g^{-1}
Pore volume, V_p / cm^3 g^{-1}
MOF-177
IRMOF1
CuBTC
MIL-100
MgMOF-74
MIL47
ZIF-8
zeolites
MOFs
FAU
BEA
LTA
CHA
MFI
MOR
DDR
MTW
TON

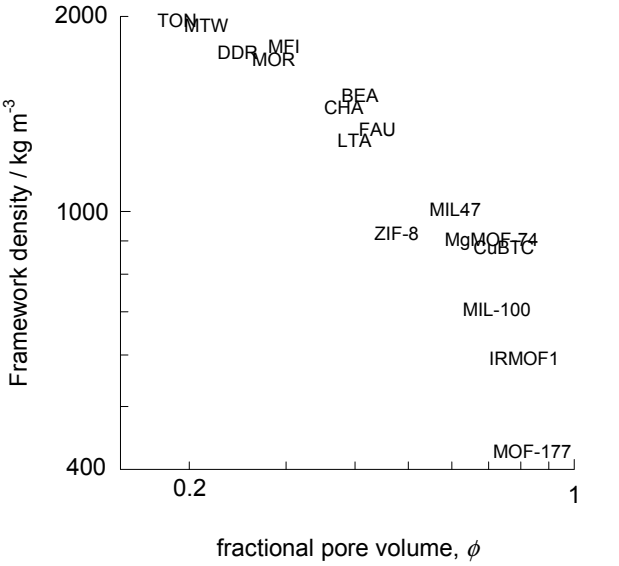
(b)
2000
1000
400
0.2
1
Framework density / kg m^{-3}
fractional pore volume, ϕ
TON
MTW
DDR
MFI
MOR
BEA
CHA
FAU
LTA
MIL47
ZIF-8
MgMOF-74
CuBTC
MIL-100
IRMOF1
MOF-177

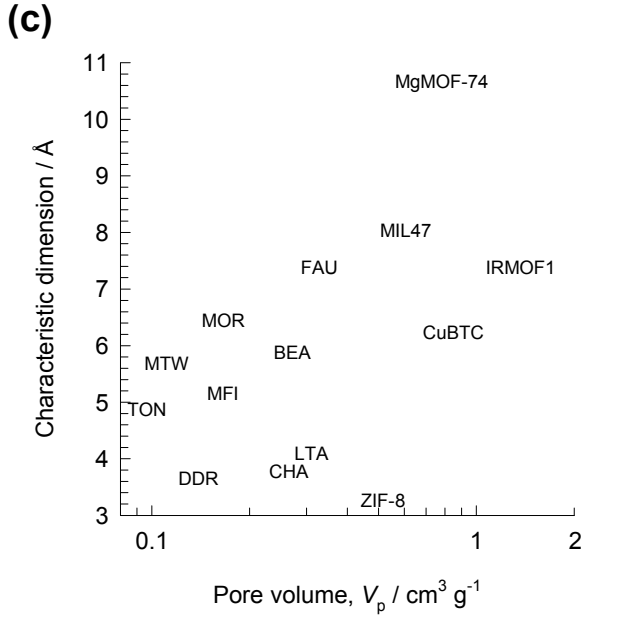
(c)
11
10
9
8
7
6
5
4
3
0.1
1
2
Characteristic dimension / Å
Pore volume, V_p / cm^3 g^{-1}
MgMOF-74
MIL47
FAU
IRMOF1
MOR
CuBTC
BEA
MTW
MFI
TON
LTA
CHA
DDR
ZIF-8

Figure 2

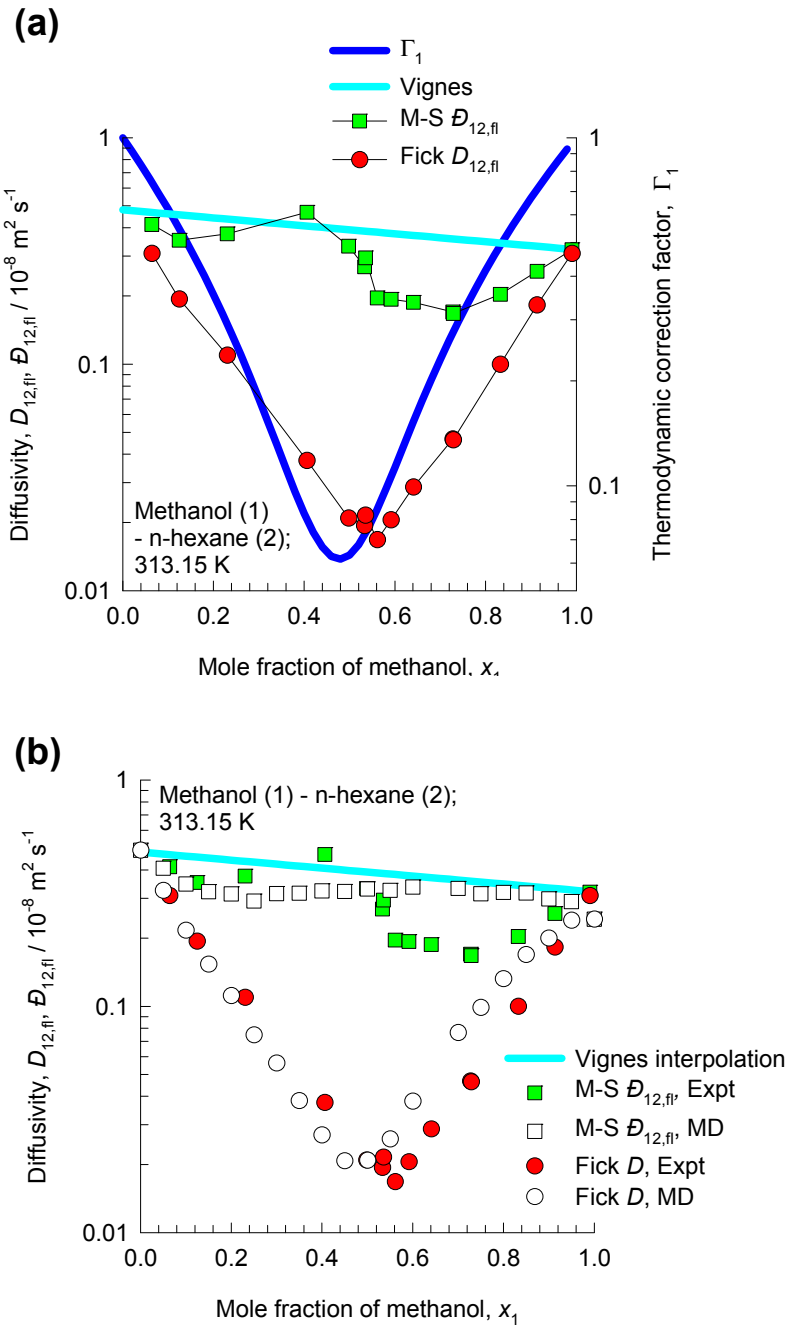
(a)
Γ1
Vignes
M-S Đ12,fl
Fick D12,fl
Methanol (1)
- n-hexane (2);
313.15 K
Diffusivity, D12,fl, Đ12,fl / 10-8 m2 s-1
Thermodynamic correction factor, Γ1
Mole fraction of methanol, x1
(b)
Methanol (1) - n-hexane (2);
313.15 K
Vignes interpolation
M-S Đ12,fl, Expt
M-S Đ12,fl, MD
Fick D, Expt
Fick D, MD
Diffusivity, D12,fl, Đ12,fl / 10-8 m2 s-1
Mole fraction of methanol, x1

Figure 3

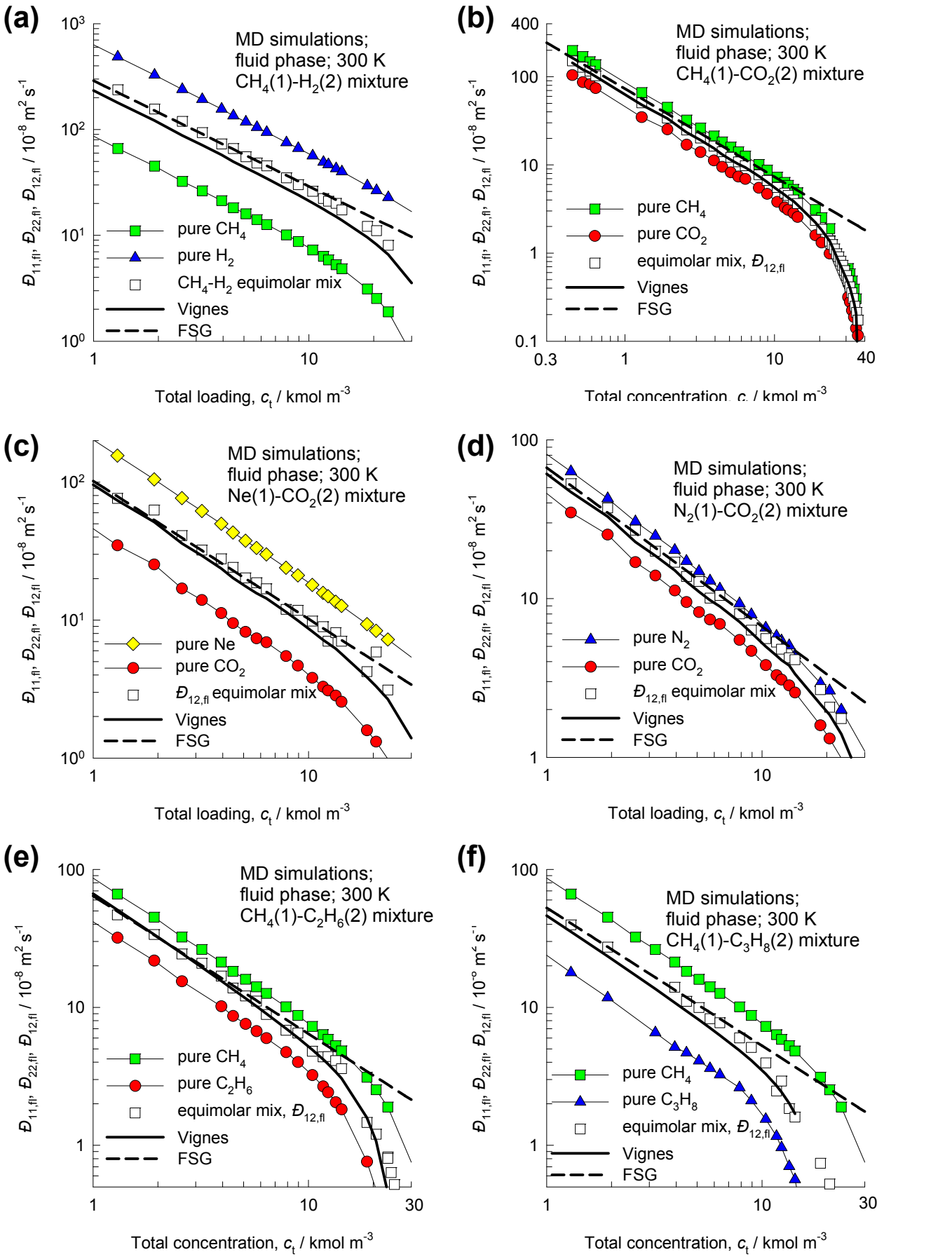
(a)
MD simulations;
fluid phase; 300 K
CH4(1)-H2(2) mixture
pure CH4
pure H2
CH4-H2 equimolar mix
Vignes
FSG
Đ11,fl, Đ22,fl, Đ12,fl / 10-8 m2 s-1
Total loading, ct / kmol m-3
(b)
MD simulations;
fluid phase; 300 K
CH4(1)-CO2(2) mixture
pure CH4
pure CO2
equimolar mix, Đ12,fl
Vignes
FSG
Đ11,fl, Đ22,fl, Đ12,fl / 10-8 m2 s-1
Total concentration, ct / kmol m-3
(c)
MD simulations;
fluid phase; 300 K
Ne(1)-CO2(2) mixture
pure Ne
pure CO2
Đ12,fl equimolar mix
Vignes
FSG
Đ11,fl, Đ22,fl, Đ12,fl / 10-8 m2 s-1
Total loading, ct / kmol m-3
(d)
MD simulations;
fluid phase; 300 K
N2(1)-CO2(2) mixture
pure N2
pure CO2
Đ12,fl equimolar mix
Vignes
FSG
Đ11,fl, Đ22,fl, Đ12,fl / 10-8 m2 s-1
Total loading, ct / kmol m-3
(e)
MD simulations;
fluid phase; 300 K
CH4(1)-C2H6(2) mixture
pure CH4
pure C2H6
equimolar mix, Đ12,fl
Vignes
FSG
Đ11,fl, Đ22,fl, Đ12,fl / 10-8 m2 s-1
Total concentration, ct / kmol m-3
(f)
MD simulations;
fluid phase; 300 K
CH4(1)-C3H8(2) mixture
pure CH4
pure C3H8
equimolar mix, Đ12,fl
Vignes
FSG
Đ11,fl, Đ22,fl, Đ12,fl / 10-8 m2 s-1
Total concentration, ct / kmol m-3

Figure 4

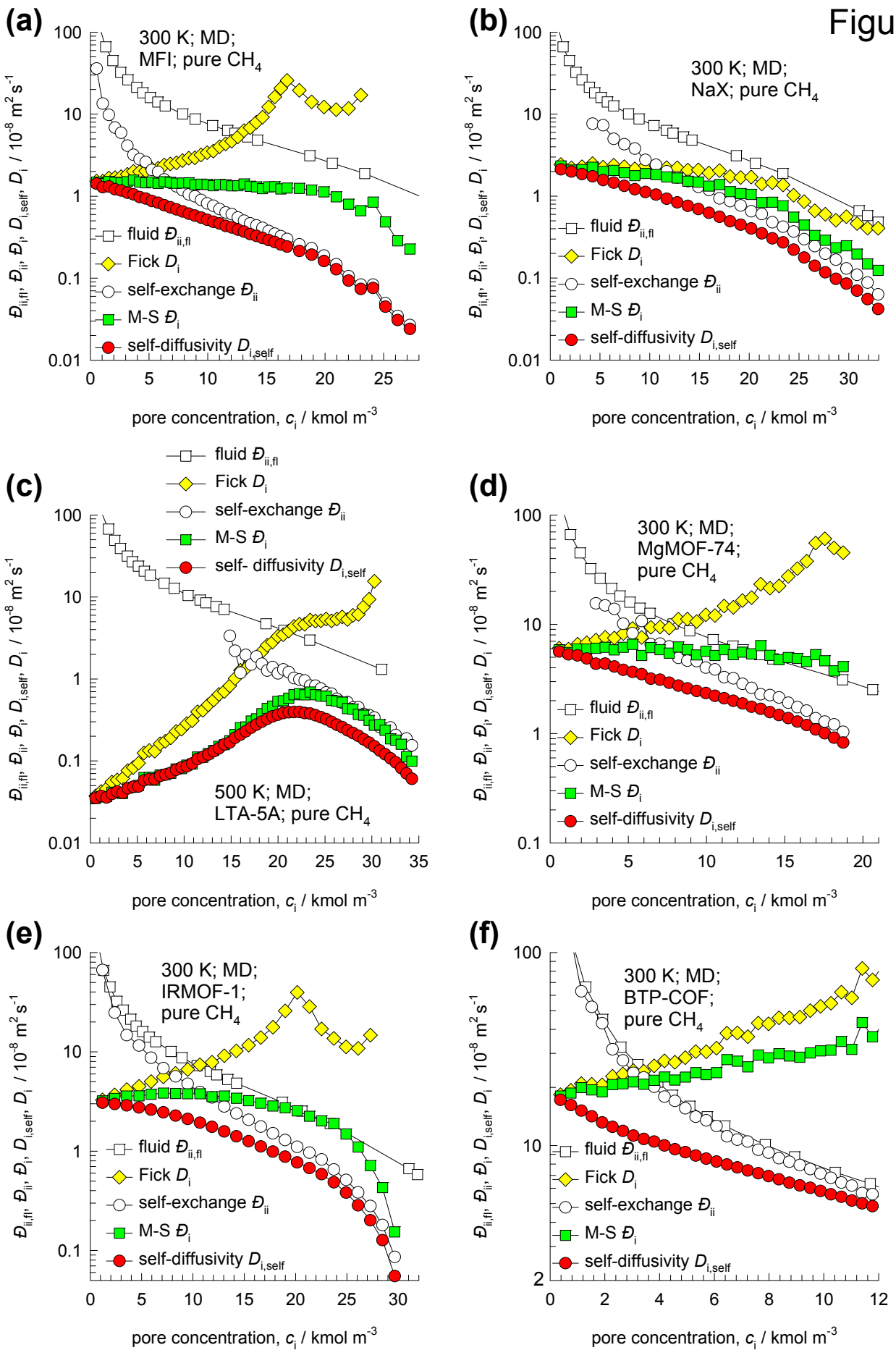
(a)
300 K; MD;
MFI; pure CH4
(b)
300 K; MD;
NaX; pure CH4
(c)
500 K; MD;
LTA-5A; pure CH4
(d)
300 K; MD;
MgMOF-74;
pure CH4
(e)
300 K; MD;
IRMOF-1;
pure CH4
(f)
300 K; MD;
BTP-COF;
pure CH4
fluid Đii,fl
Fick Di
self-exchange Đii
M-S Đi
self-diffusivity Di,self
self- diffusivity Di,self
Đii,fl, Đii, Đi, Di,self, Di / 10-8 m2 s-1
pore concentration, ci / kmol m-3

Figure 5

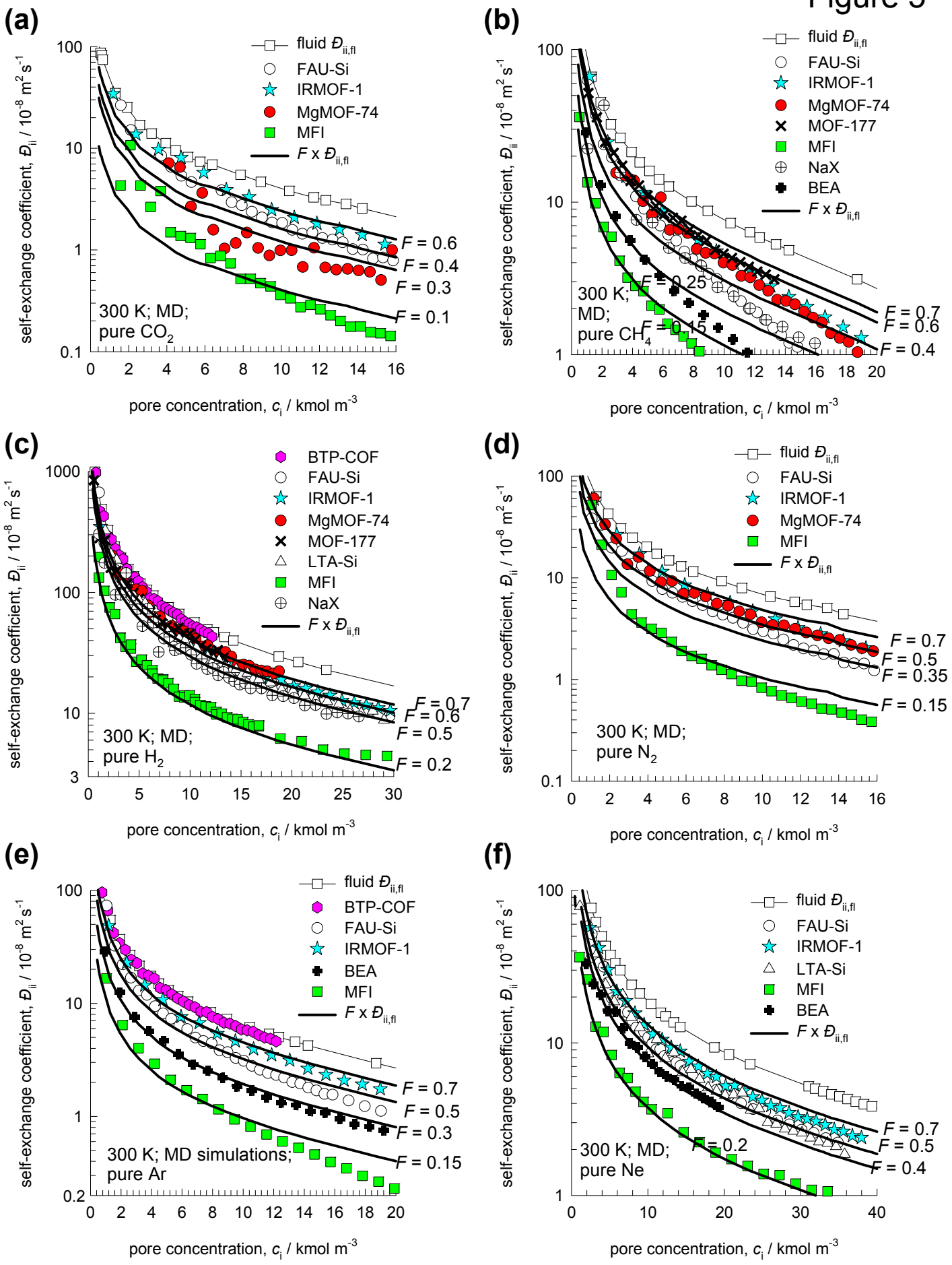
(a)
self-exchange coefficient, Đii / 10-8 m2 s-1
pore concentration, ci / kmol m-3
fluid Đii,fl
FAU-Si
IRMOF-1
MgMOF-74
MFI
F x Đii,fl
F = 0.6
F = 0.4
F = 0.3
F = 0.1
300 K; MD;
pure CO2
(b)
fluid Đii,fl
FAU-Si
IRMOF-1
MgMOF-74
MOF-177
MFI
NaX
BEA
F x Đii,fl
F = 0.25
F = 0.15
F = 0.7
F = 0.6
F = 0.4
300 K;
MD;
pure CH4
(c)
BTP-COF
FAU-Si
IRMOF-1
MgMOF-74
MOF-177
LTA-Si
MFI
NaX
F x Đii,fl
F = 0.7
F = 0.6
F = 0.5
F = 0.2
300 K; MD;
pure H2
(d)
fluid Đii,fl
FAU-Si
IRMOF-1
MgMOF-74
MFI
F x Đii,fl
F = 0.7
F = 0.5
F = 0.35
F = 0.15
300 K; MD;
pure N2
(e)
fluid Đii,fl
BTP-COF
FAU-Si
IRMOF-1
BEA
MFI
F x Đii,fl
F = 0.7
F = 0.5
F = 0.3
F = 0.15
300 K; MD simulations;
pure Ar
(f)
fluid Đii,fl
FAU-Si
IRMOF-1
LTA-Si
MFI
BEA
F x Đii,fl
F = 0.7
F = 0.5
F = 0.4
F = 0.2
300 K; MD;
pure Ne

Figure 6

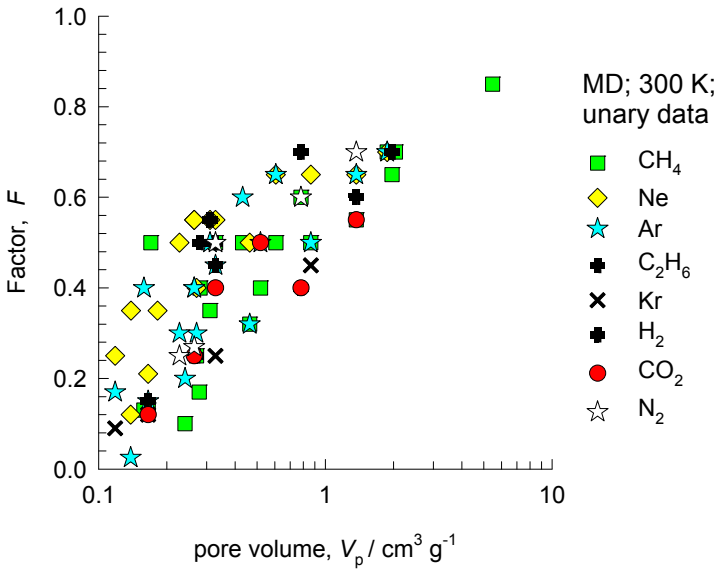
1.0
0.8
0.6
0.4
0.2
0.0
Factor, F
0.1
1
10
pore volume, V_p / cm^3 g^{-1}
MD; 300 K;
unary data
CH_4
Ne
Ar
C_2H_6
Kr
H_2
CO_2
N_2

Figure 7

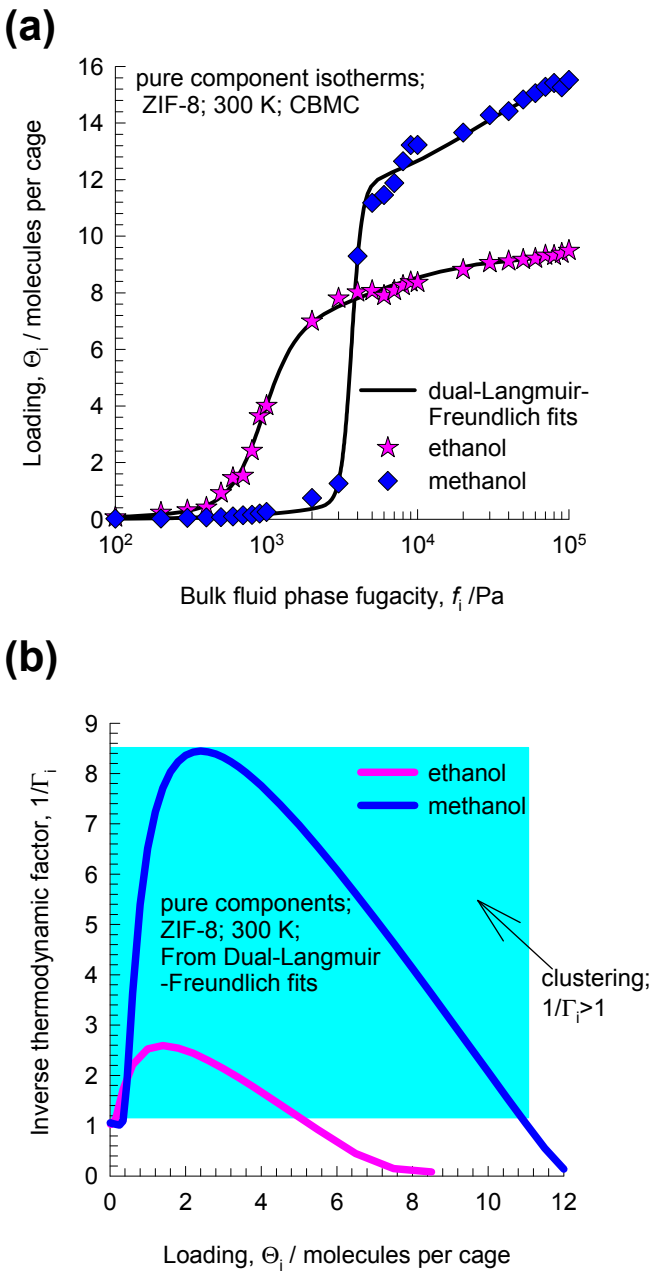
(a)
pure component isotherms;
ZIF-8; 300 K; CBMC
Loading, Θi / molecules per cage
Bulk fluid phase fugacity, fi /Pa
dual-Langmuir-Freundlich fits
ethanol
methanol
(b)
Inverse thermodynamic factor, 1/Γi
Loading, Θi / molecules per cage
ethanol
methanol
pure components;
ZIF-8; 300 K;
From Dual-Langmuir
-Freundlich fits
clustering;
1/Γi>1

Figure 8

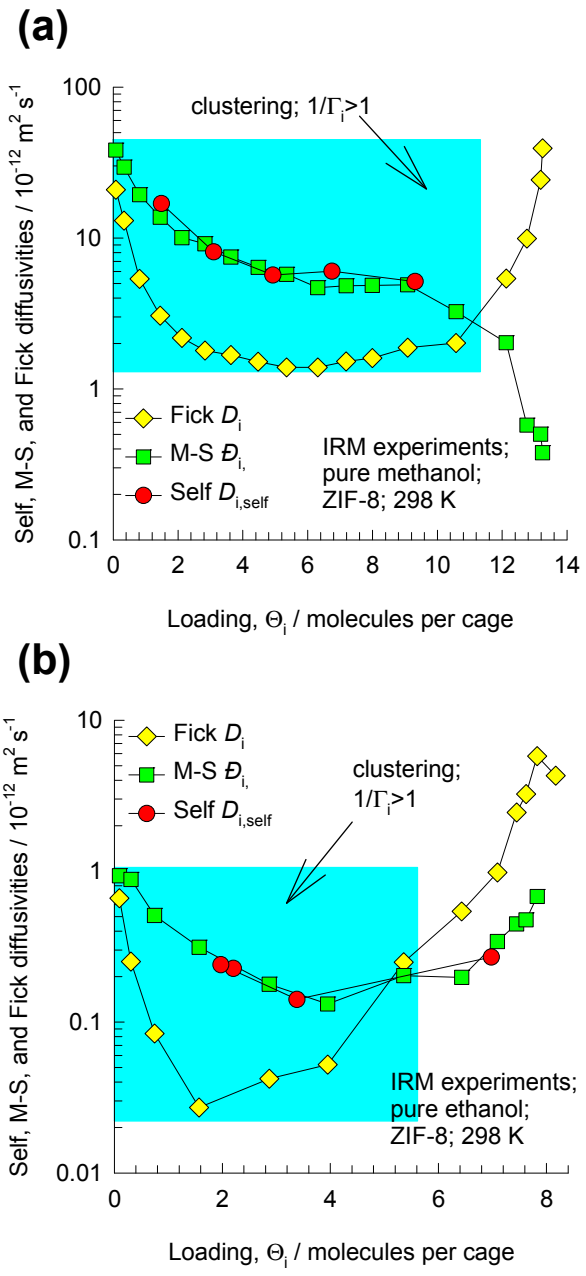
(a)
clustering; 1/Γi>1
Fick Di
M-S Đi,
Self Di,self
IRM experiments;
pure methanol;
ZIF-8; 298 K
Self, M-S, and Fick diffusivities / 10-12 m2 s-1
Loading, Θi / molecules per cage
(b)
Fick Di
M-S Đi,
Self Di,self
clustering;
1/Γi>1
IRM experiments;
pure ethanol;
ZIF-8; 298 K
Self, M-S, and Fick diffusivities / 10-12 m2 s-1
Loading, Θi / molecules per cage

Figure 9

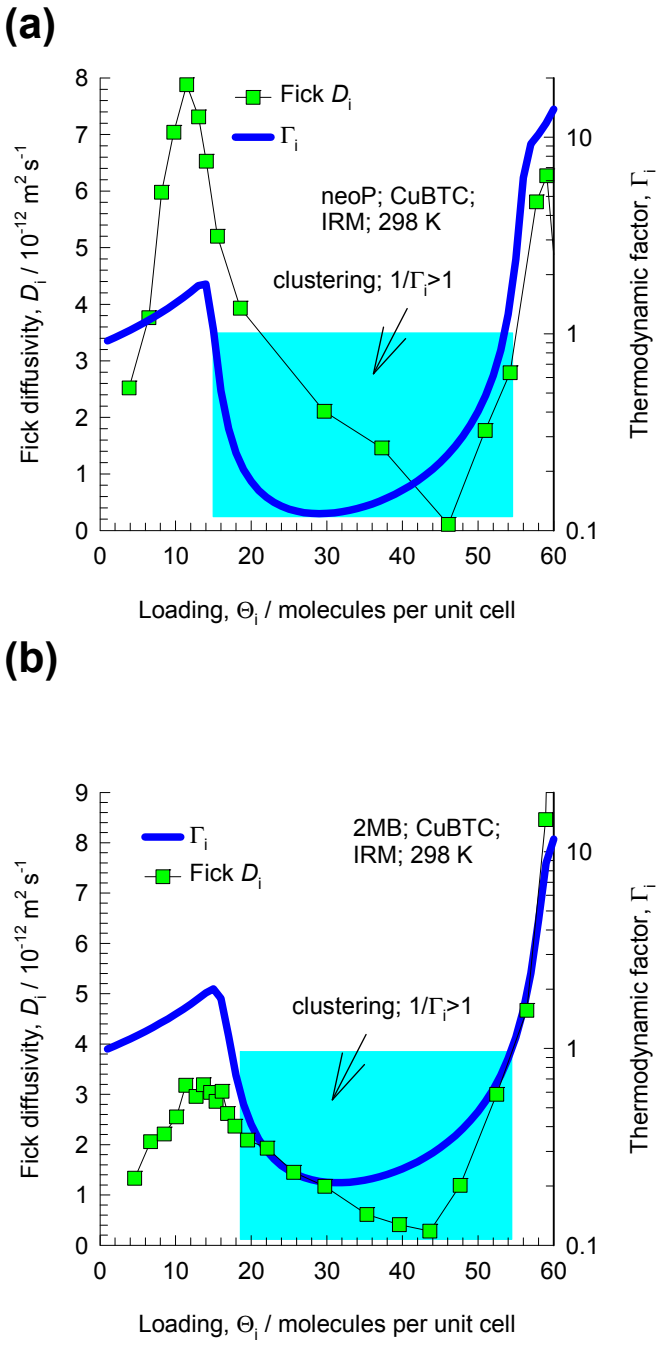
(a)
Fick D_i
Γ_i
neoP; CuBTC;
IRM; 298 K
clustering; $1/\Gamma_i>1$
Fick diffusivity, D_i / 10^{-12} m^2 s^{-1}
Thermodynamic factor, Γ_i
Loading, Θ_i / molecules per unit cell
(b)
Γ_i
Fick D_i
2MB; CuBTC;
IRM; 298 K
clustering; $1/\Gamma_i>1$
Fick diffusivity, D_i / 10^{-12} m^2 s^{-1}
Thermodynamic factor, Γ_i
Loading, Θ_i / molecules per unit cell

Figure 10

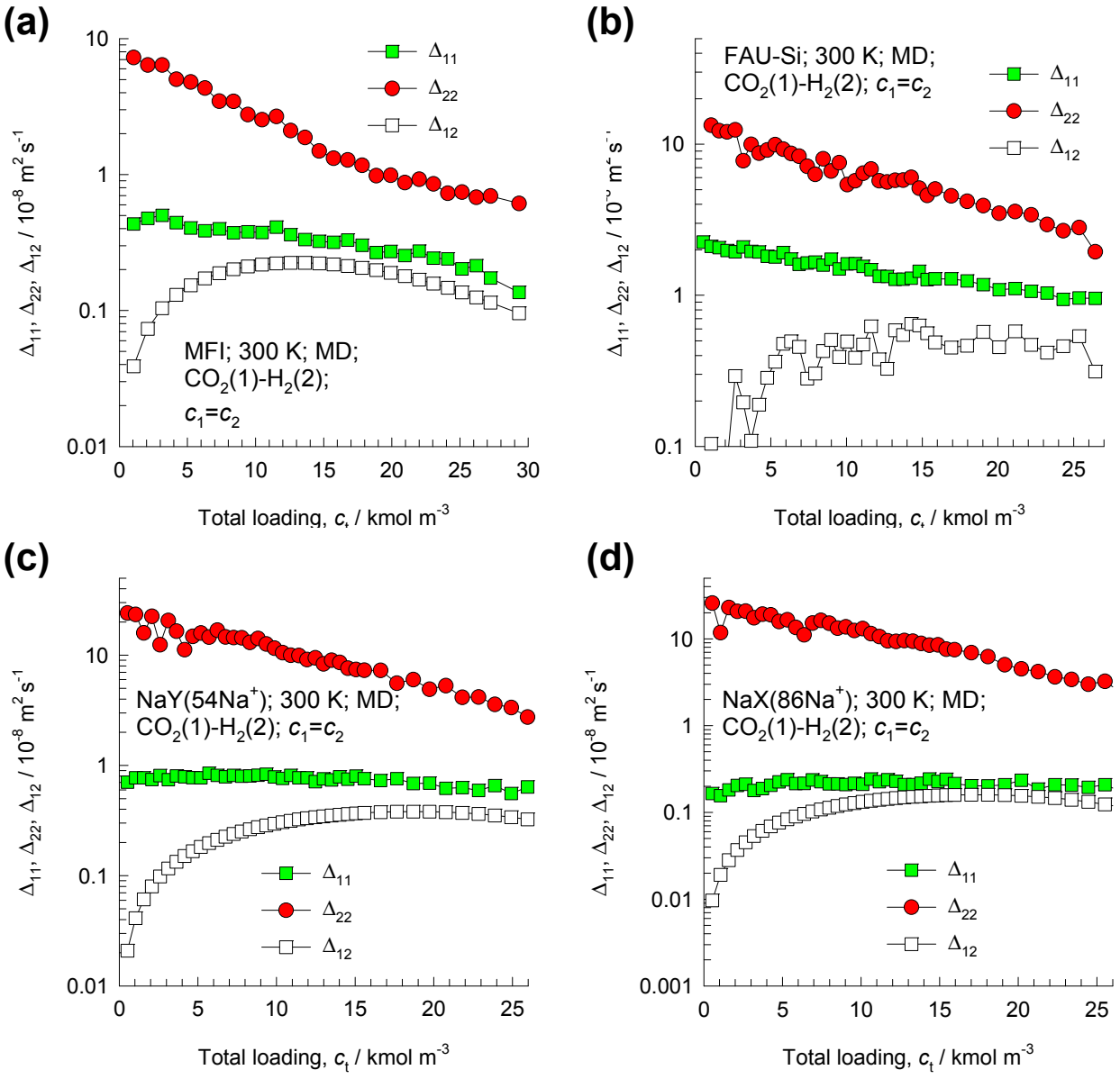
(a)
MFI; 300 K; MD;
CO2(1)-H2(2);
c1=c2
Δ11
Δ22
Δ12
Δ11, Δ22, Δ12 / 10-8 m2 s-1
Total loading, ct / kmol m-3
(b)
FAU-Si; 300 K; MD;
CO2(1)-H2(2); c1=c2
Δ11
Δ22
Δ12
Δ11, Δ22, Δ12 / 10-8 m2 s-1
Total loading, ct / kmol m-3
(c)
NaY(54Na+); 300 K; MD;
CO2(1)-H2(2); c1=c2
Δ11
Δ22
Δ12
Δ11, Δ22, Δ12 / 10-8 m2 s-1
Total loading, ct / kmol m-3
(d)
NaX(86Na+); 300 K; MD;
CO2(1)-H2(2); c1=c2
Δ11
Δ22
Δ12
Δ11, Δ22, Δ12 / 10-8 m2 s-1
Total loading, ct / kmol m-3

Figure 11

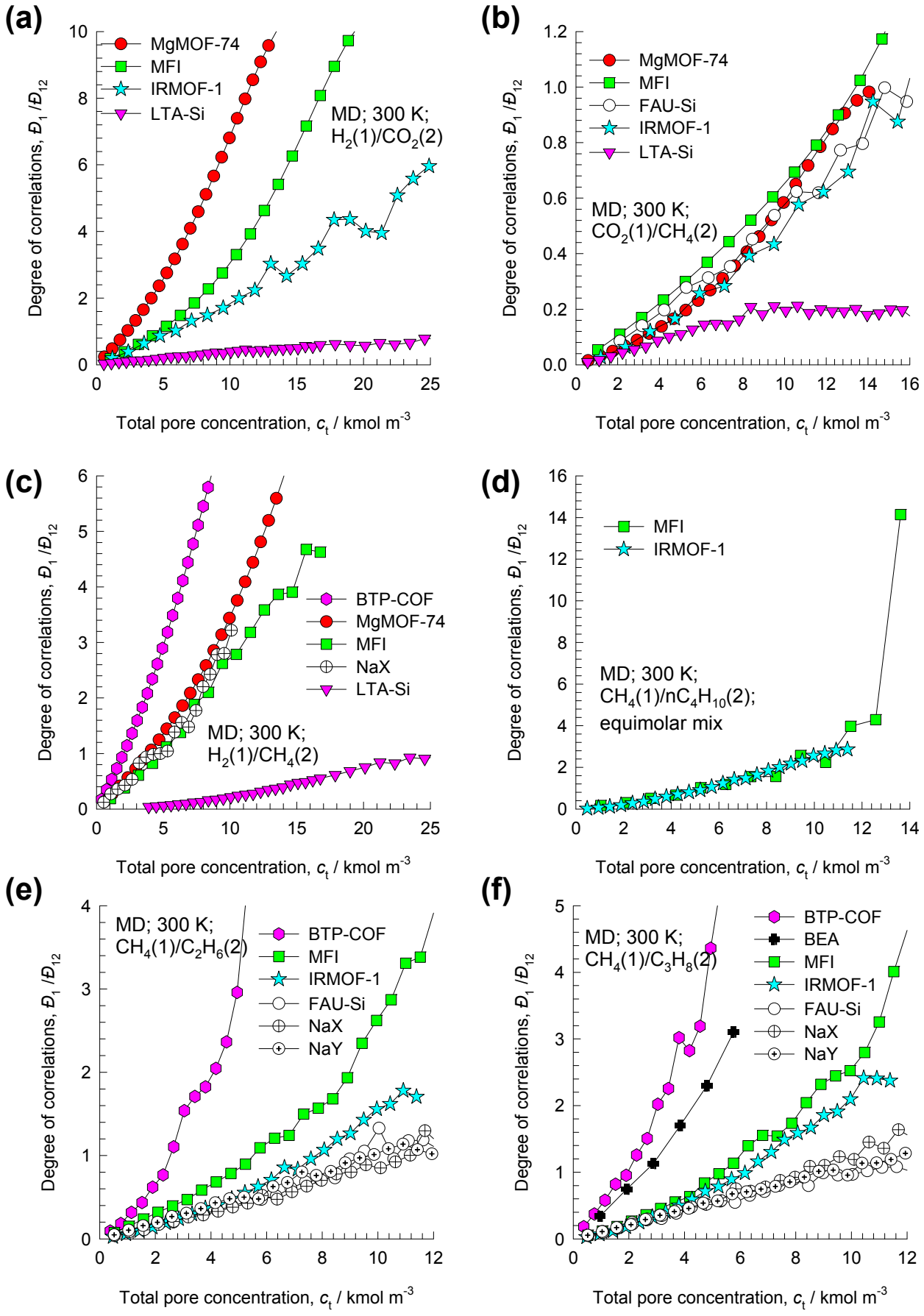
(a)
MgMOF-74
MFI
IRMOF-1
LTA-Si
MD; 300 K;
H2(1)/CO2(2)
Degree of correlations, Đ1 /Đ12
Total pore concentration, ct / kmol m-3
(b)
MgMOF-74
MFI
FAU-Si
IRMOF-1
LTA-Si
MD; 300 K;
CO2(1)/CH4(2)
Degree of correlations, Đ1 /Đ12
Total pore concentration, ct / kmol m-3
(c)
BTP-COF
MgMOF-74
MFI
NaX
LTA-Si
MD; 300 K;
H2(1)/CH4(2)
Degree of correlations, Đ1 /Đ12
Total pore concentration, ct / kmol m-3
(d)
MFI
IRMOF-1
MD; 300 K;
CH4(1)/nC4H10(2);
equimolar mix
Degree of correlations, Đ1 /Đ12
Total pore concentration, ct / kmol m-3
(e)
MD; 300 K;
CH4(1)/C2H6(2)
BTP-COF
MFI
IRMOF-1
FAU-Si
NaX
NaY
Degree of correlations, Đ1 /Đ12
Total pore concentration, ct / kmol m-3
(f)
MD; 300 K;
CH4(1)/C3H8(2)
BTP-COF
BEA
MFI
IRMOF-1
FAU-Si
NaX
NaY
Degree of correlations, Đ1 /Đ12
Total pore concentration, ct / kmol m-3

Figure 12

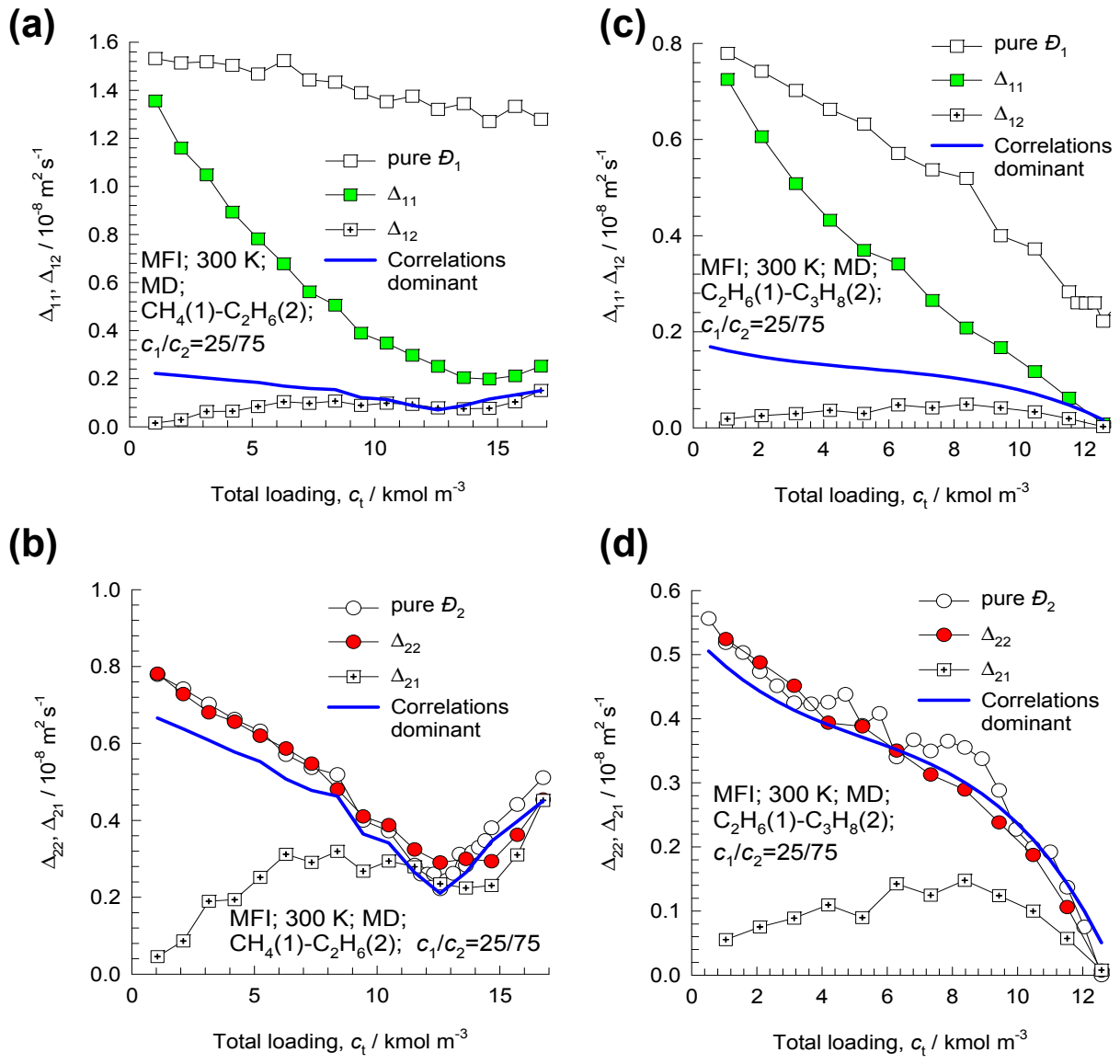
(a)
pure Đ1
Δ11
Δ12
Correlations dominant
MFI; 300 K; MD; CH4(1)-C2H6(2); c1/c2=25/75
Δ11, Δ12 / 10-8 m2 s-1
Total loading, ct / kmol m-3
(c)
pure Đ1
Δ11
Δ12
Correlations dominant
MFI; 300 K; MD; C2H6(1)-C3H8(2); c1/c2=25/75
Δ11, Δ12 / 10-8 m2 s-1
Total loading, ct / kmol m-3
(b)
pure Đ2
Δ22
Δ21
Correlations dominant
MFI; 300 K; MD; CH4(1)-C2H6(2); c1/c2=25/75
Δ22, Δ21 / 10-8 m2 s-1
Total loading, ct / kmol m-3
(d)
pure Đ2
Δ22
Δ21
Correlations dominant
MFI; 300 K; MD; C2H6(1)-C3H8(2); c1/c2=25/75
Δ22, Δ21 / 10-8 m2 s-1
Total loading, ct / kmol m-3

Figure 13

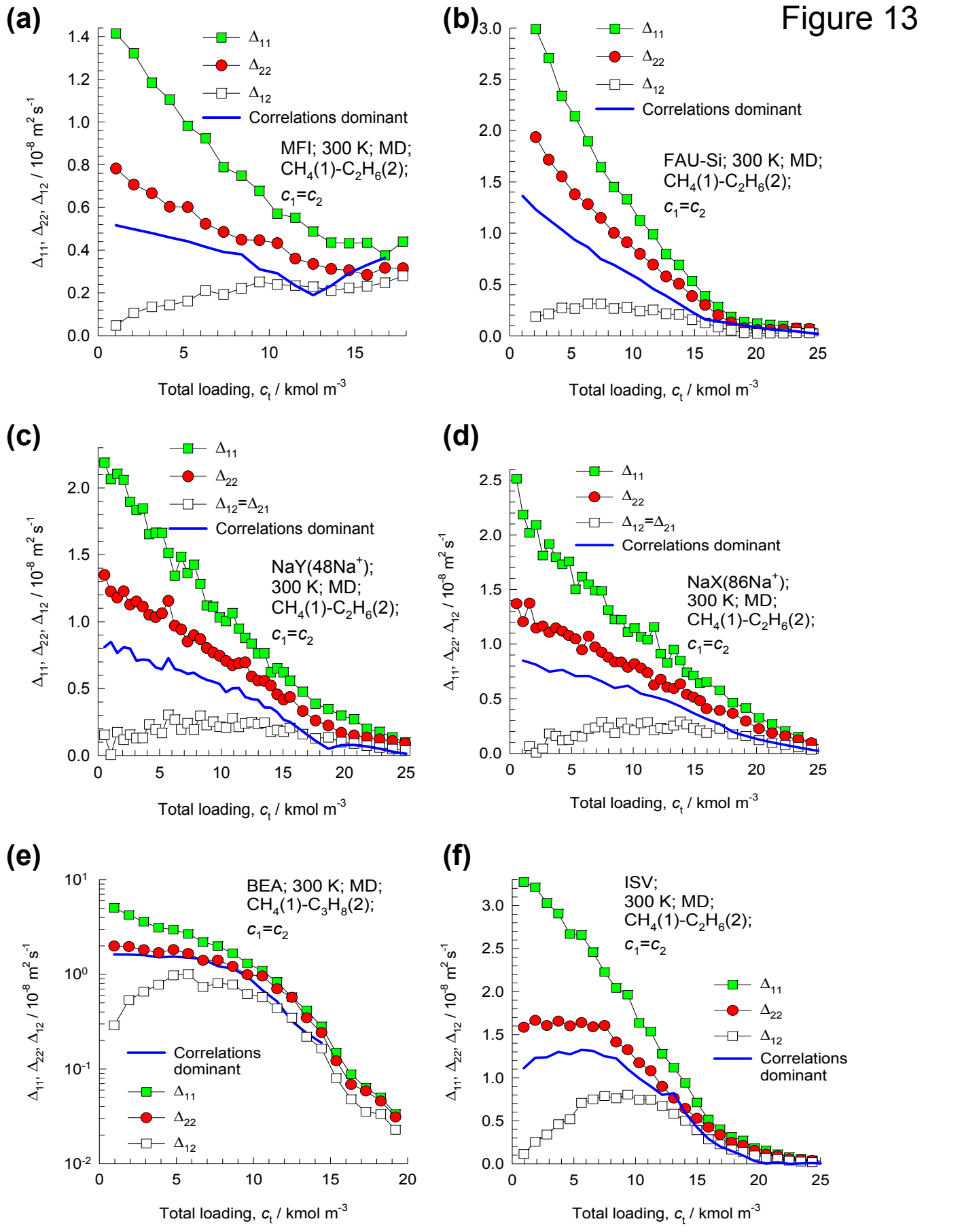
(a)
MFI; 300 K; MD;
CH4(1)-C2H6(2);
c1=c2
Correlations dominant
(b)
FAU-Si; 300 K; MD;
CH4(1)-C2H6(2);
c1=c2
Correlations dominant
(c)
NaY(48Na+);
300 K; MD;
CH4(1)-C2H6(2);
c1=c2
Correlations dominant
(d)
NaX(86Na+);
300 K; MD;
CH4(1)-C2H6(2);
c1=c2
Correlations dominant
(e)
BEA; 300 K; MD;
CH4(1)-C3H8(2);
c1=c2
Correlations dominant
(f)
ISV;
300 K; MD;
CH4(1)-C2H6(2);
c1=c2
Correlations dominant
Δ11
Δ22
Δ12
Δ12=Δ21
Δ11, Δ22, Δ12 / 10-8 m2 s-1
Total loading, ct / kmol m-3

Figure 14

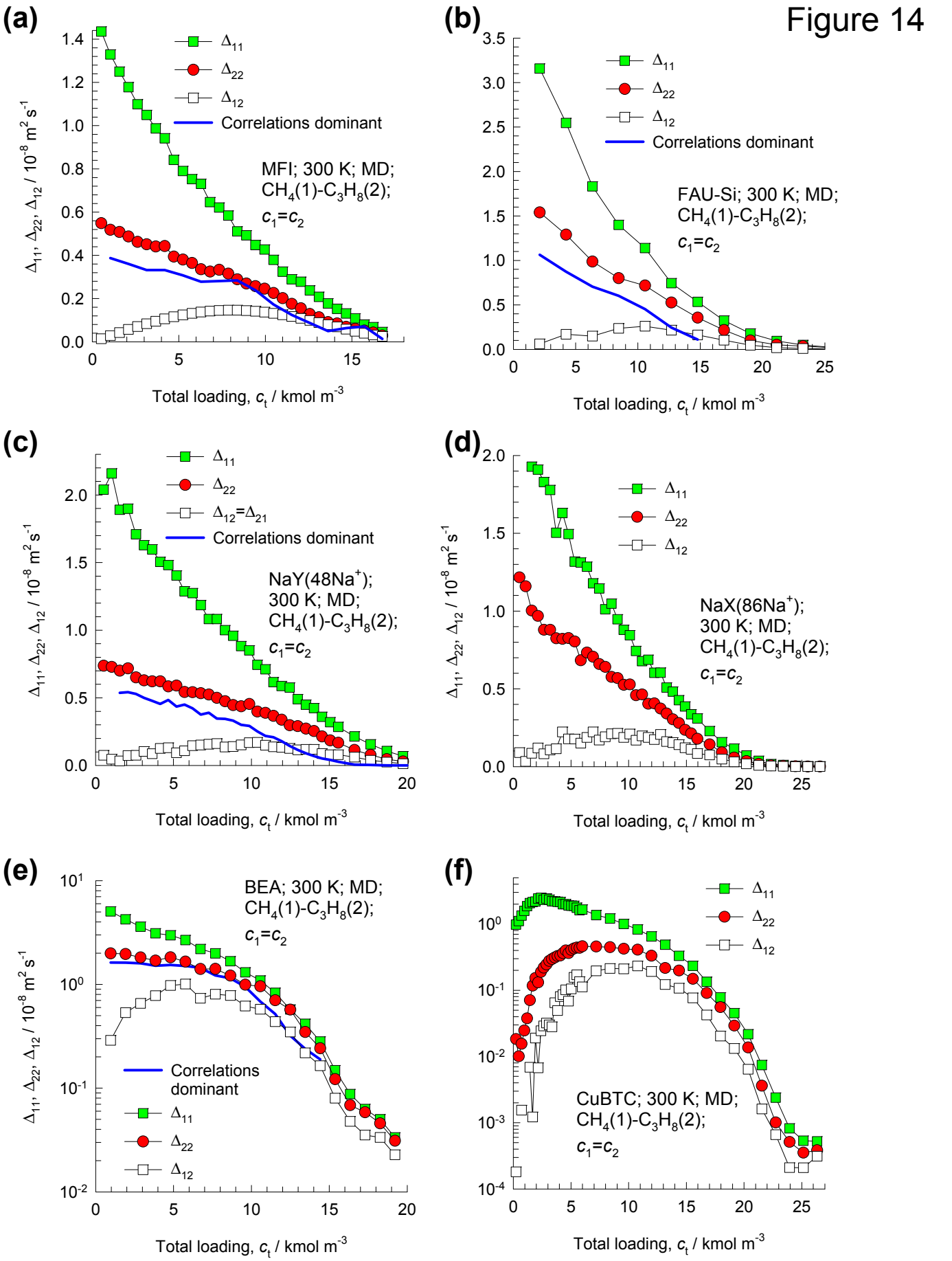
(a)
Δ11
Δ22
Δ12
Correlations dominant
MFI; 300 K; MD;
CH4(1)-C3H8(2);
c1=c2
Δ11, Δ22, Δ12 / 10-8 m2 s-1
Total loading, ct / kmol m-3
(b)
Δ11
Δ22
Δ12
Correlations dominant
FAU-Si; 300 K; MD;
CH4(1)-C3H8(2);
c1=c2
Total loading, ct / kmol m-3
(c)
Δ11
Δ22
Δ12=Δ21
Correlations dominant
NaY(48Na+);
300 K; MD;
CH4(1)-C3H8(2);
c1=c2
Δ11, Δ22, Δ12 / 10-8 m2 s-1
Total loading, ct / kmol m-3
(d)
Δ11
Δ22
Δ12
NaX(86Na+);
300 K; MD;
CH4(1)-C3H8(2);
c1=c2
Δ11, Δ22, Δ12 / 10-8 m2 s-1
Total loading, ct / kmol m-3
(e)
BEA; 300 K; MD;
CH4(1)-C3H8(2);
c1=c2
Correlations
dominant
Δ11
Δ22
Δ12
Δ11, Δ22, Δ12 / 10-8 m2 s-1
Total loading, ct / kmol m-3
(f)
Δ11
Δ22
Δ12
CuBTC; 300 K; MD;
CH4(1)-C3H8(2);
c1=c2
Total loading, ct / kmol m-3

Figure 15

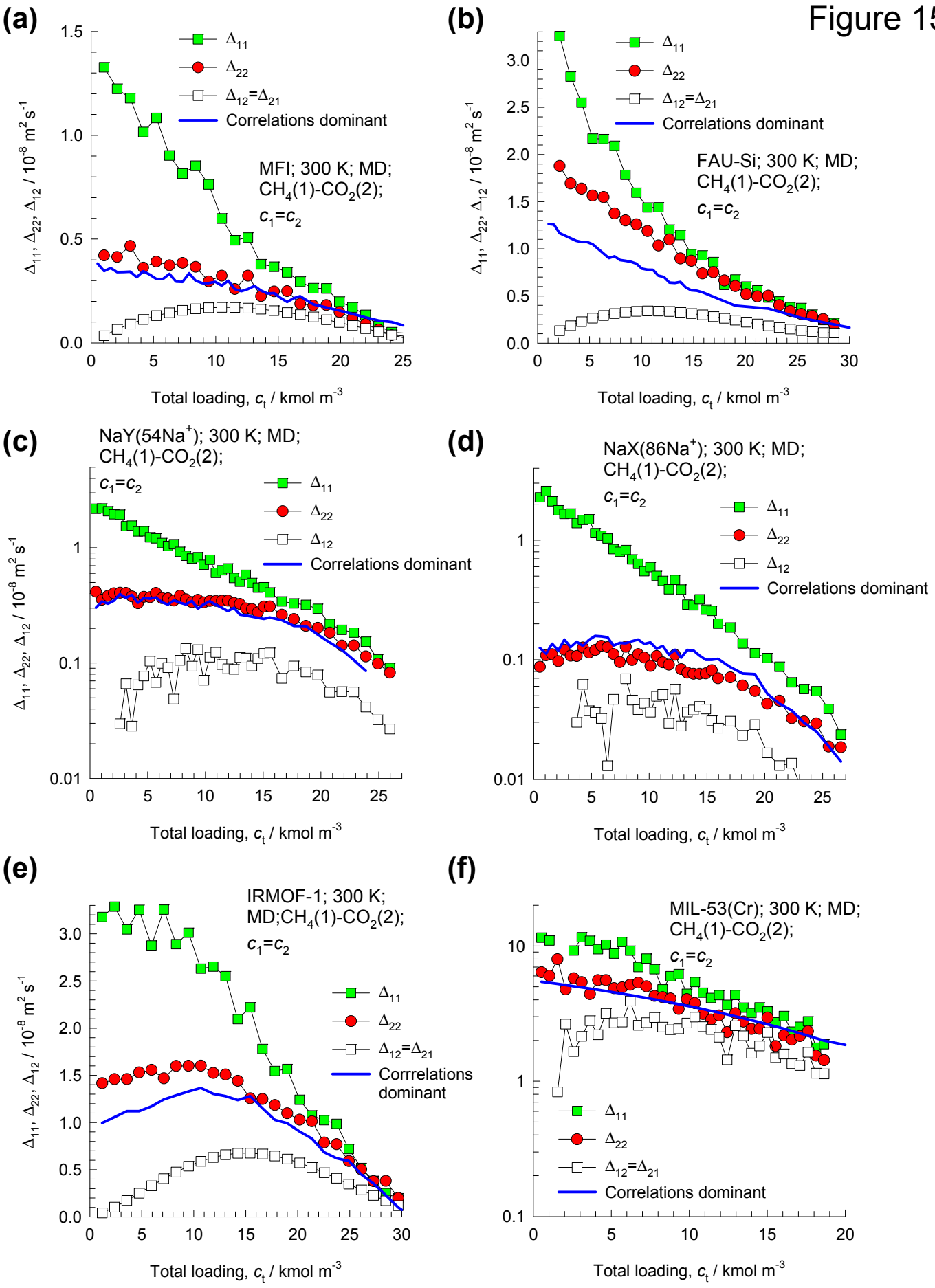
(a)
MFI; 300 K; MD;
CH4(1)-CO2(2);
c1=c2
Δ11
Δ22
Δ12=Δ21
Correlations dominant
Δ11, Δ22, Δ12 / 10-8 m2 s-1
Total loading, ct / kmol m-3
(b)
FAU-Si; 300 K; MD;
CH4(1)-CO2(2);
c1=c2
Δ11
Δ22
Δ12=Δ21
Correlations dominant
Δ11, Δ22, Δ12 / 10-8 m2 s-1
Total loading, ct / kmol m-3
(c)
NaY(54Na+); 300 K; MD;
CH4(1)-CO2(2);
c1=c2
Δ11
Δ22
Δ12
Correlations dominant
Δ11, Δ22, Δ12 / 10-8 m2 s-1
Total loading, ct / kmol m-3
(d)
NaX(86Na+); 300 K; MD;
CH4(1)-CO2(2);
c1=c2
Δ11
Δ22
Δ12
Correlations dominant
Total loading, ct / kmol m-3
(e)
IRMOF-1; 300 K;
MD;CH4(1)-CO2(2);
c1=c2
Δ11
Δ22
Δ12=Δ21
Corrrelations
dominant
Δ11, Δ22, Δ12 / 10-8 m2 s-1
Total loading, ct / kmol m-3
(f)
MIL-53(Cr); 300 K; MD;
CH4(1)-CO2(2);
c1=c2
Δ11
Δ22
Δ12=Δ21
Correlations dominant
Total loading, ct / kmol m-3

Figure 16

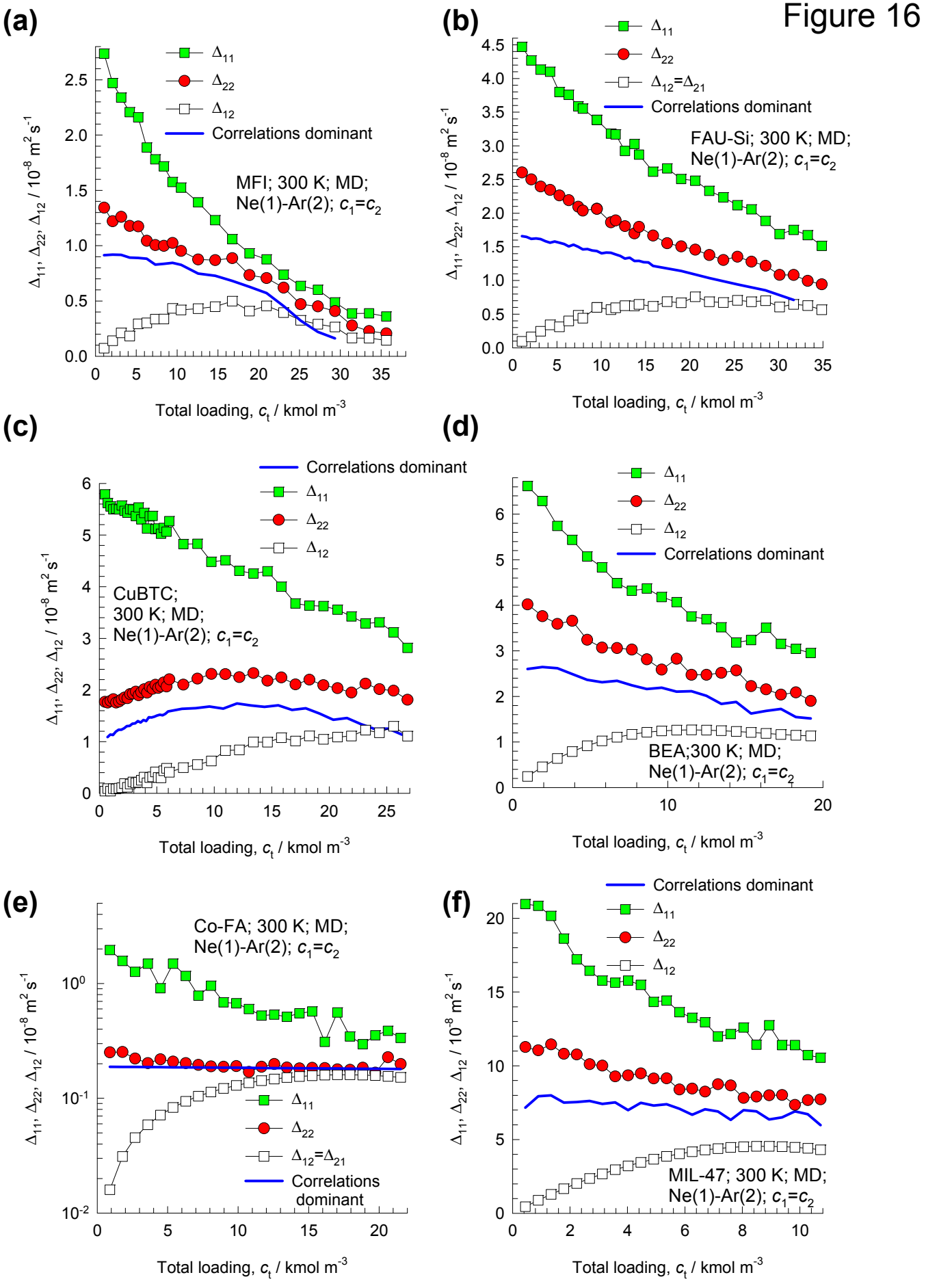
(a)
MFI; 300 K; MD;
Ne(1)-Ar(2); c_1=c_2
(b)
FAU-Si; 300 K; MD;
Ne(1)-Ar(2); c_1=c_2
(c)
CuBTC;
300 K; MD;
Ne(1)-Ar(2); c_1=c_2
(d)
BEA;300 K; MD;
Ne(1)-Ar(2); c_1=c_2
(e)
Co-FA; 300 K; MD;
Ne(1)-Ar(2); c_1=c_2
(f)
MIL-47; 300 K; MD;
Ne(1)-Ar(2); c_1=c_2
Δ_{11}
Δ_{22}
Δ_{12}
Δ_{12}=Δ_{21}
Correlations dominant
Δ_{11}, Δ_{22}, Δ_{12} / 10^{-8} m^2 s^{-1}
Total loading, c_t / kmol m^{-3}

Figure 17

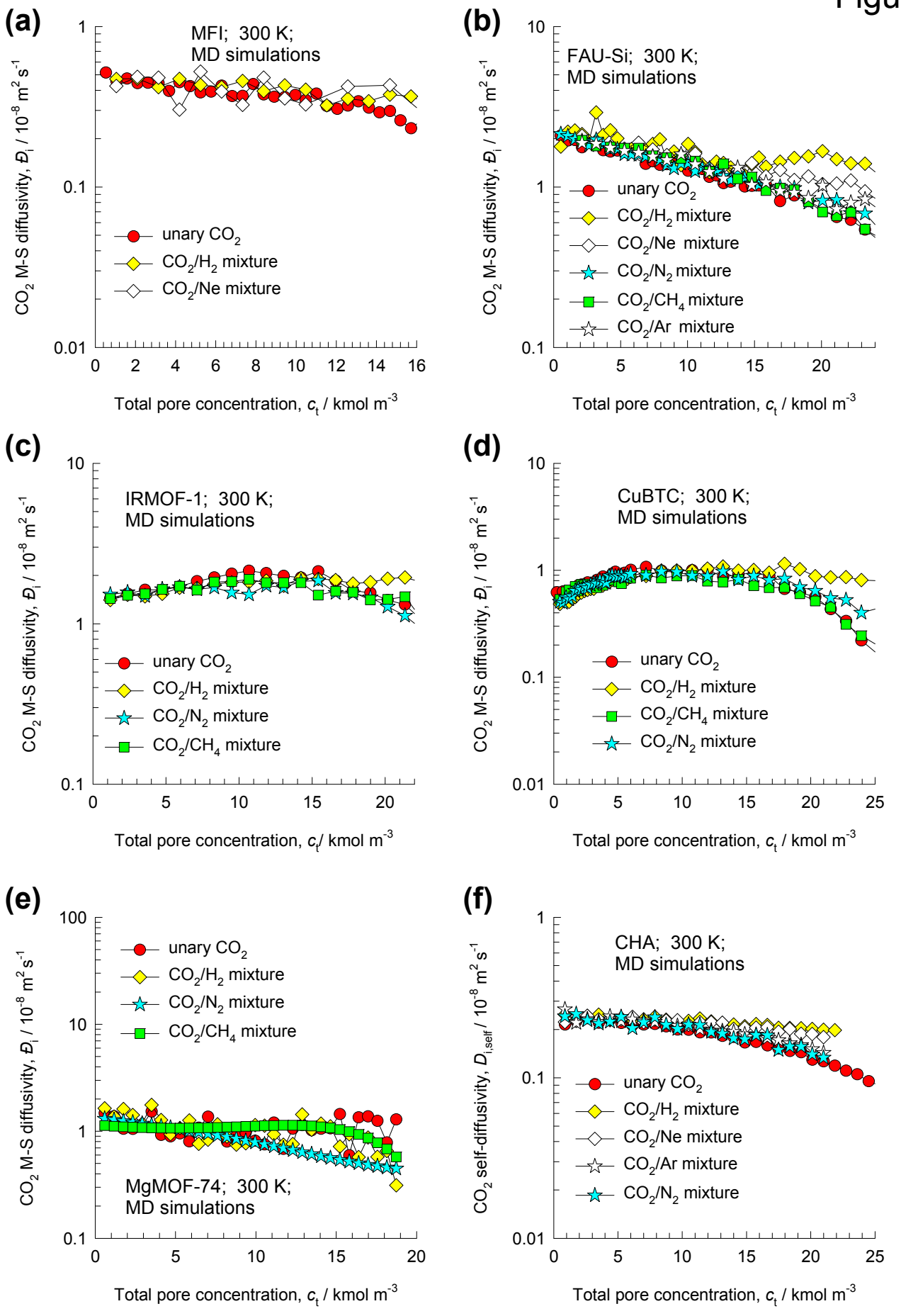
(a)
MFI; 300 K;
MD simulations
unary CO2
CO2/H2 mixture
CO2/Ne mixture
CO2 M-S diffusivity, Đi / 10-8 m2 s-1
Total pore concentration, ct / kmol m-3
(b)
FAU-Si; 300 K;
MD simulations
unary CO2
CO2/H2 mixture
CO2/Ne mixture
CO2/N2 mixture
CO2/CH4 mixture
CO2/Ar mixture
CO2 M-S diffusivity, Đi / 10-8 m2 s-1
Total pore concentration, ct / kmol m-3
(c)
IRMOF-1; 300 K;
MD simulations
unary CO2
CO2/H2 mixture
CO2/N2 mixture
CO2/CH4 mixture
CO2 M-S diffusivity, Đi / 10-8 m2 s-1
Total pore concentration, ct / kmol m-3
(d)
CuBTC; 300 K;
MD simulations
unary CO2
CO2/H2 mixture
CO2/CH4 mixture
CO2/N2 mixture
CO2 M-S diffusivity, Đi / 10-8 m2 s-1
Total pore concentration, ct / kmol m-3
(e)
unary CO2
CO2/H2 mixture
CO2/N2 mixture
CO2/CH4 mixture
MgMOF-74; 300 K;
MD simulations
CO2 M-S diffusivity, Đi / 10-8 m2 s-1
Total pore concentration, ct / kmol m-3
(f)
CHA; 300 K;
MD simulations
unary CO2
CO2/H2 mixture
CO2/Ne mixture
CO2/Ar mixture
CO2/N2 mixture
CO2 self-diffusivity, Di,self / 10-8 m2 s-1
Total pore concentration, ct / kmol m-3

Figure 18

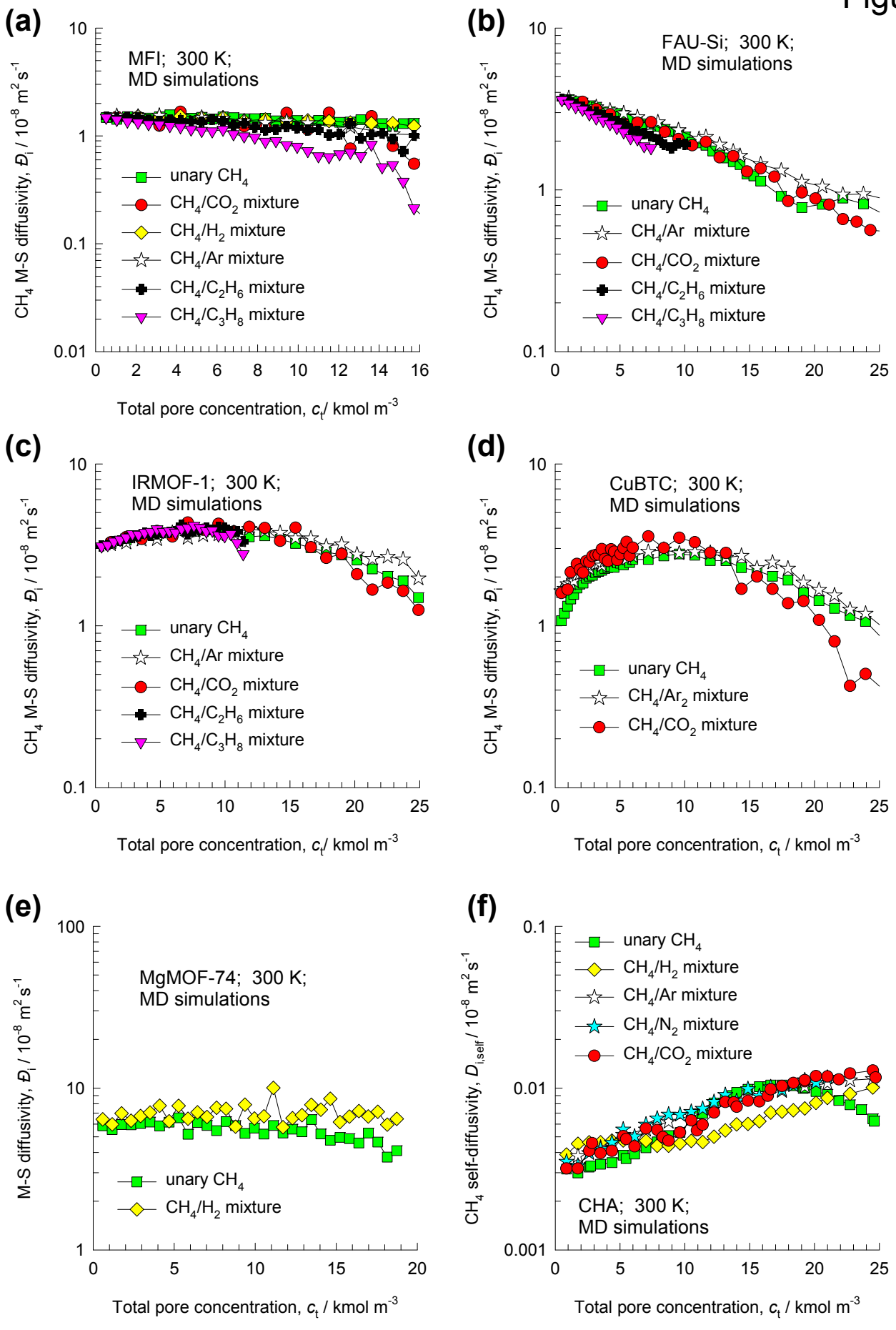
(a)
MFI; 300 K;
MD simulations
unary CH4
CH4/CO2 mixture
CH4/H2 mixture
CH4/Ar mixture
CH4/C2H6 mixture
CH4/C3H8 mixture
CH4 M-S diffusivity, Đi / 10-8 m2 s-1
Total pore concentration, ct/ kmol m-3
(b)
FAU-Si; 300 K;
MD simulations
unary CH4
CH4/Ar mixture
CH4/CO2 mixture
CH4/C2H6 mixture
CH4/C3H8 mixture
CH4 M-S diffusivity, Đi / 10-8 m2 s-1
(c)
IRMOF-1; 300 K;
MD simulations
unary CH4
CH4/Ar mixture
CH4/CO2 mixture
CH4/C2H6 mixture
CH4/C3H8 mixture
CH4 M-S diffusivity, Đi / 10-8 m2 s-1
Total pore concentration, ct/ kmol m-3
(d)
CuBTC; 300 K;
MD simulations
unary CH4
CH4/Ar2 mixture
CH4/CO2 mixture
CH4 M-S diffusivity, Đi / 10-8 m2 s-1
Total pore concentration, ct / kmol m-3
(e)
MgMOF-74; 300 K;
MD simulations
unary CH4
CH4/H2 mixture
M-S diffusivity, Đi / 10-8 m2 s-1
Total pore concentration, ct / kmol m-3
(f)
unary CH4
CH4/H2 mixture
CH4/Ar mixture
CH4/N2 mixture
CH4/CO2 mixture
CHA; 300 K;
MD simulations
CH4 self-diffusivity, Di,self / 10-8 m2 s-1
Total pore concentration, ct / kmol m-3

Figure 19

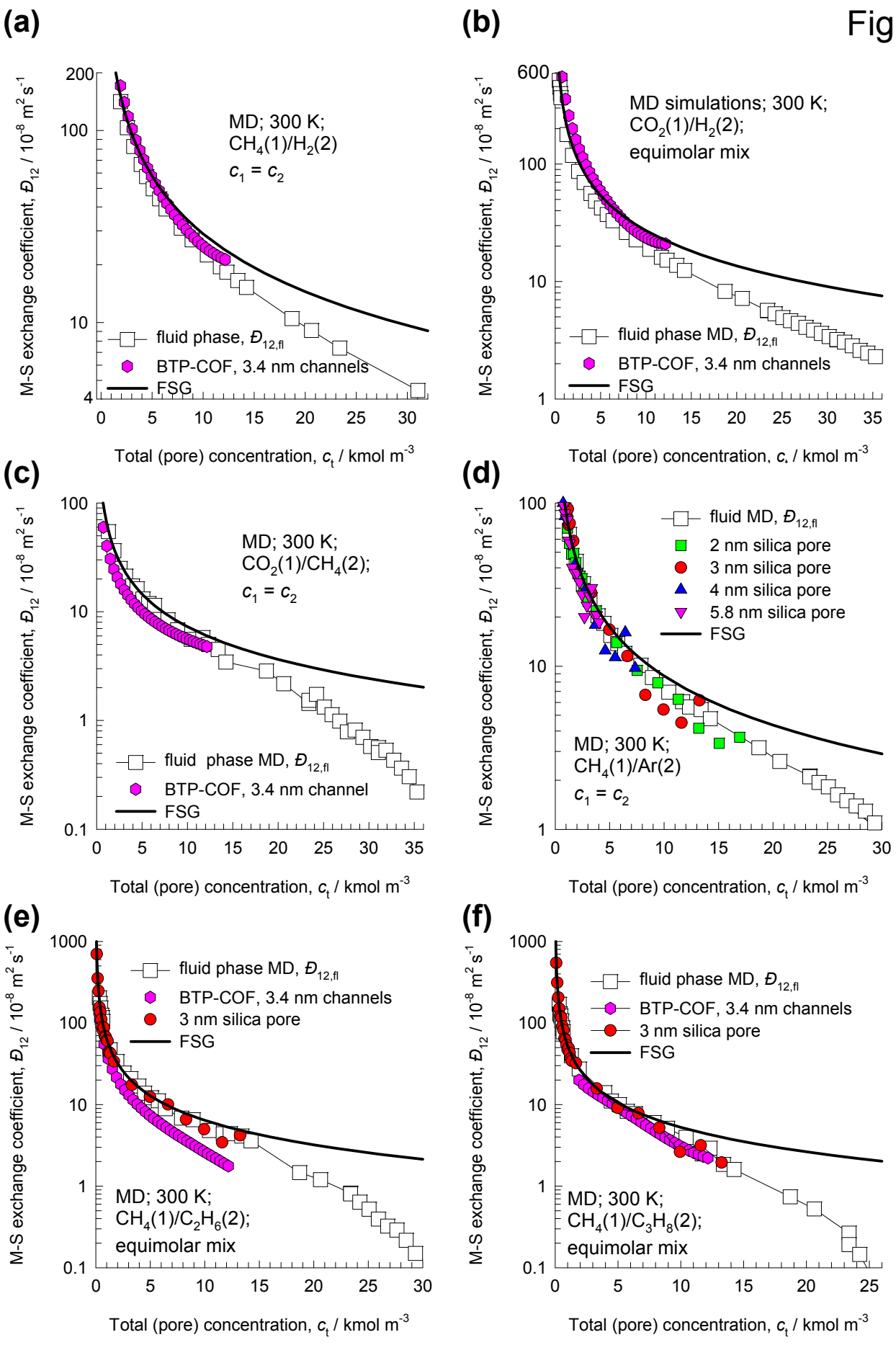
(a)
MD; 300 K;
CH4(1)/H2(2)
c1 = c2
fluid phase, Đ12,fl
BTP-COF, 3.4 nm channels
FSG
M-S exchange coefficient, Đ12 / 10-8 m2 s-1
Total (pore) concentration, ct / kmol m-3
(b)
MD simulations; 300 K;
CO2(1)/H2(2);
equimolar mix
fluid phase MD, Đ12,fl
BTP-COF, 3.4 nm channels
FSG
(c)
MD; 300 K;
CO2(1)/CH4(2);
c1 = c2
fluid phase MD, Đ12,fl
BTP-COF, 3.4 nm channel
FSG
(d)
fluid MD, Đ12,fl
2 nm silica pore
3 nm silica pore
4 nm silica pore
5.8 nm silica pore
FSG
MD; 300 K;
CH4(1)/Ar(2)
c1 = c2
(e)
fluid phase MD, Đ12,fl
BTP-COF, 3.4 nm channels
3 nm silica pore
FSG
MD; 300 K;
CH4(1)/C2H6(2);
equimolar mix
(f)
fluid phase MD, Đ12,fl
BTP-COF, 3.4 nm channels
3 nm silica pore
FSG
MD; 300 K;
CH4(1)/C3H8(2);
equimolar mix

Figure 20

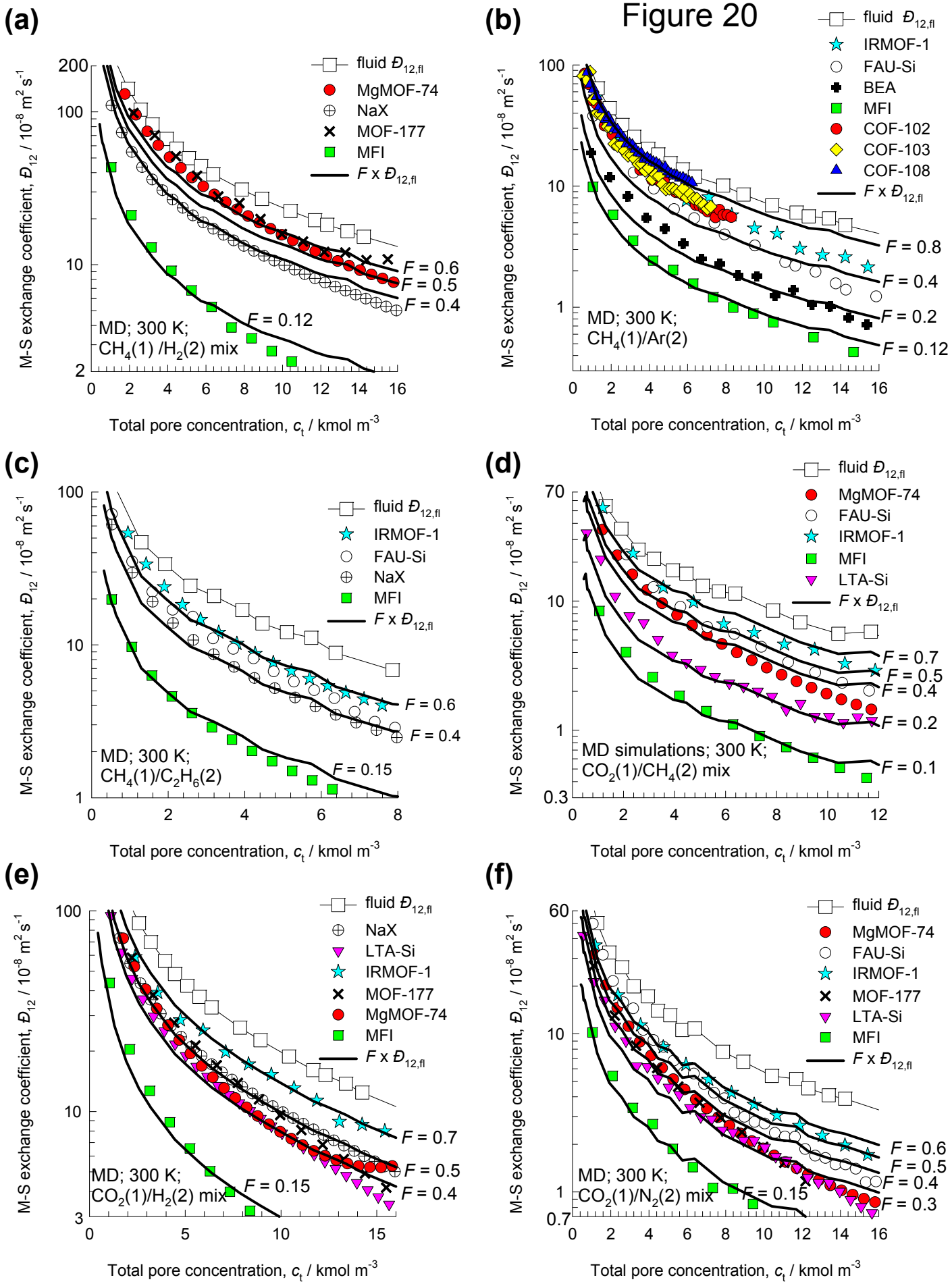
(a)
fluid Đ12,fl
MgMOF-74
NaX
MOF-177
MFI
F x Đ12,fl
F = 0.6
F = 0.5
F = 0.4
F = 0.12
MD; 300 K;
CH4(1) /H2(2) mix
M-S exchange coefficient, Đ12 / 10-8 m2 s-1
Total pore concentration, ct / kmol m-3
(b)
fluid Đ12,fl
IRMOF-1
FAU-Si
BEA
MFI
COF-102
COF-103
COF-108
F x Đ12,fl
F = 0.8
F = 0.4
F = 0.2
F = 0.12
MD; 300 K;
CH4(1)/Ar(2)
M-S exchange coefficient, Đ12 / 10-8 m2 s-1
Total pore concentration, ct / kmol m-3
(c)
fluid Đ12,fl
IRMOF-1
FAU-Si
NaX
MFI
F x Đ12,fl
F = 0.6
F = 0.4
F = 0.15
MD; 300 K;
CH4(1)/C2H6(2)
M-S exchange coefficient, Đ12 / 10-8 m2 s-1
Total pore concentration, ct / kmol m-3
(d)
fluid Đ12,fl
MgMOF-74
FAU-Si
IRMOF-1
MFI
LTA-Si
F x Đ12,fl
F = 0.7
F = 0.5
F = 0.4
F = 0.2
F = 0.1
MD simulations; 300 K;
CO2(1)/CH4(2) mix
M-S exchange coefficient, Đ12 / 10-8 m2 s-1
Total pore concentration, ct / kmol m-3
(e)
fluid Đ12,fl
NaX
LTA-Si
IRMOF-1
MOF-177
MgMOF-74
MFI
F x Đ12,fl
F = 0.7
F = 0.5
F = 0.4
F = 0.15
MD; 300 K;
CO2(1)/H2(2) mix
M-S exchange coefficient, Đ12 / 10-8 m2 s-1
Total pore concentration, ct / kmol m-3
(f)
fluid Đ12,fl
MgMOF-74
FAU-Si
IRMOF-1
MOF-177
LTA-Si
MFI
F x Đ12,fl
F = 0.6
F = 0.5
F = 0.4
F = 0.3
F = 0.15
MD; 300 K;
CO2(1)/N2(2) mix
M-S exchange coefficient, Đ12 / 10-8 m2 s-1
Total pore concentration, ct / kmol m-3

Figure 21

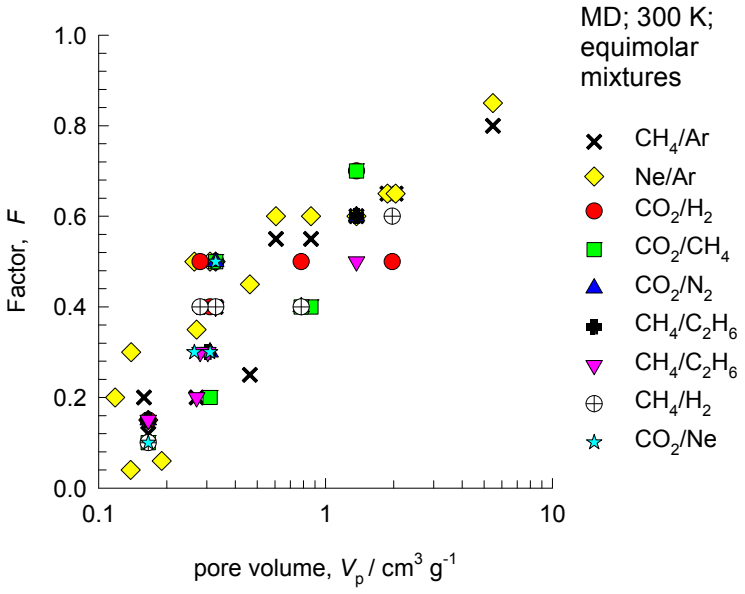
MD; 300 K;
equimolar
mixtures
CH4/Ar
Ne/Ar
CO2/H2
CO2/CH4
CO2/N2
CH4/C2H6
CH4/C2H6
CH4/H2
CO2/Ne
Factor, F
1.0
0.8
0.6
0.4
0.2
0.0
0.1
1
10
pore volume, Vp / cm3 g-1

Figure 22

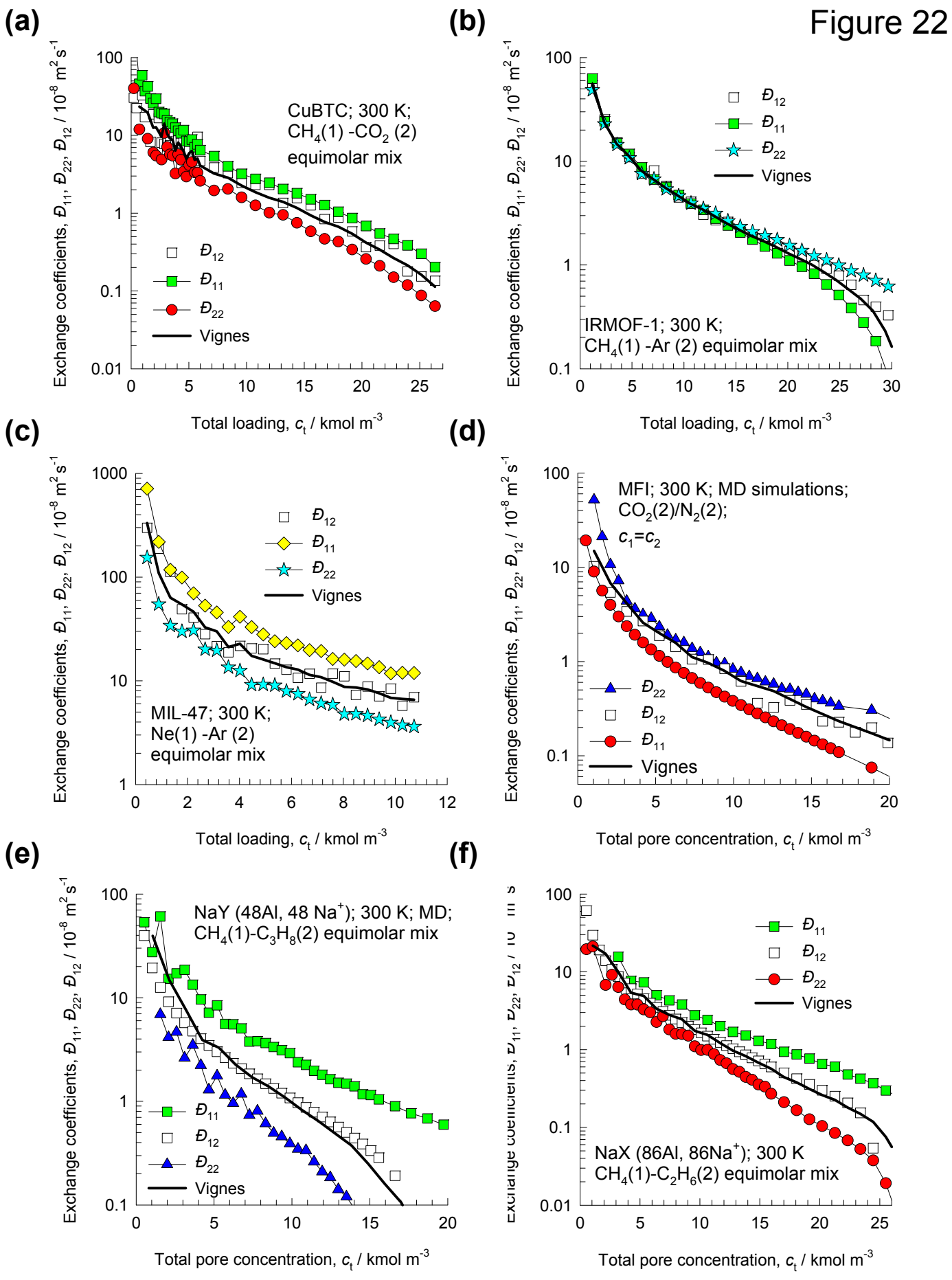
(a)
CuBTC; 300 K;
CH4(1) -CO2 (2)
equimolar mix
Đ12
Đ11
Đ22
Vignes
Exchange coefficients, Đ11, Đ22, Đ12 / 10-8 m2 s-1
Total loading, ct / kmol m-3
(b)
IRMOF-1; 300 K;
CH4(1) -Ar (2) equimolar mix
(c)
MIL-47; 300 K;
Ne(1) -Ar (2)
equimolar mix
(d)
MFI; 300 K; MD simulations;
CO2(2)/N2(2);
c1=c2
Total pore concentration, ct / kmol m-3
(e)
NaY (48Al, 48 Na+); 300 K; MD;
CH4(1)-C3H8(2) equimolar mix
(f)
NaX (86Al, 86Na+); 300 K
CH4(1)-C2H6(2) equimolar mix

Figure 23

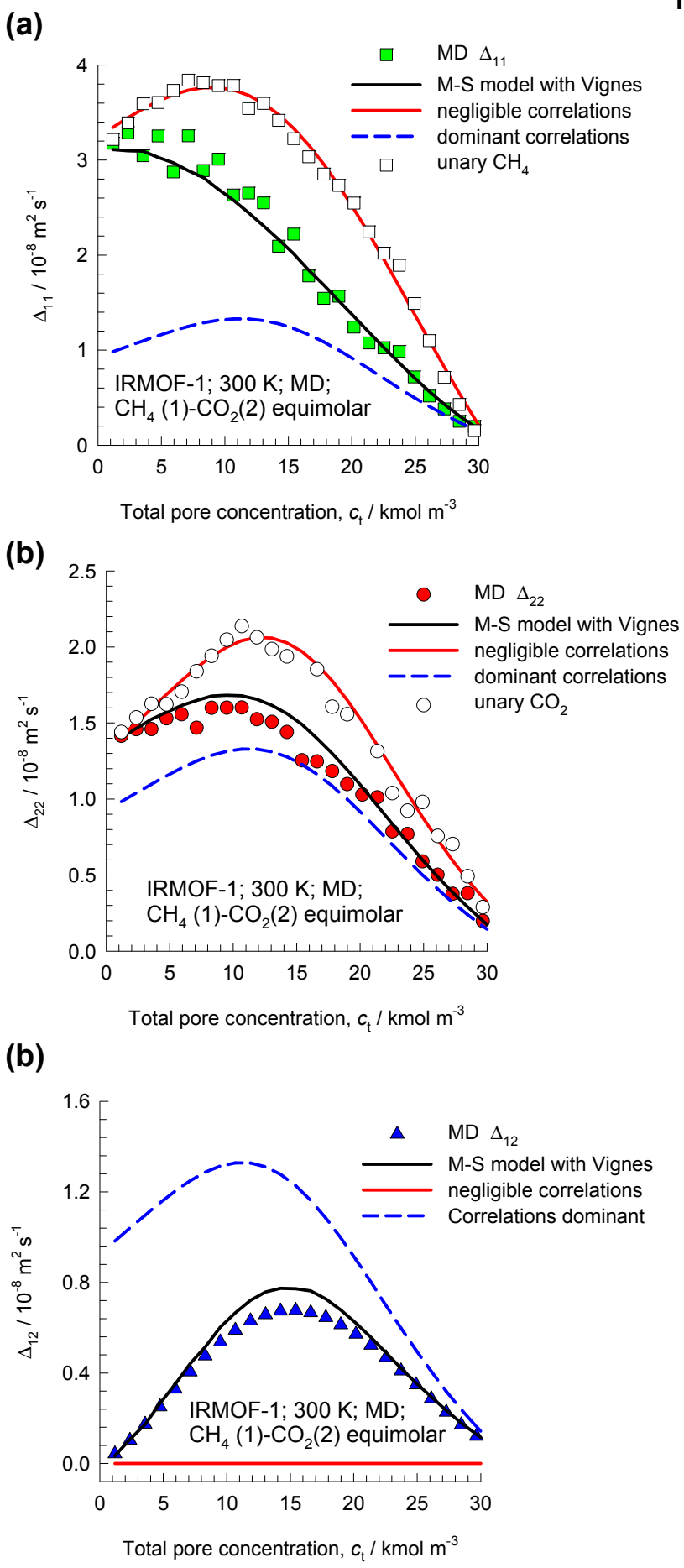
(a)
MD Δ11
M-S model with Vignes
negligible correlations
dominant correlations
unary CH4
IRMOF-1; 300 K; MD;
CH4 (1)-CO2(2) equimolar
Δ11 / 10-8 m2 s-1
Total pore concentration, ct / kmol m-3
(b)
MD Δ22
M-S model with Vignes
negligible correlations
dominant correlations
unary CO2
IRMOF-1; 300 K; MD;
CH4 (1)-CO2(2) equimolar
Δ22 / 10-8 m2 s-1
Total pore concentration, ct / kmol m-3
(b)
MD Δ12
M-S model with Vignes
negligible correlations
Correlations dominant
IRMOF-1; 300 K; MD;
CH4 (1)-CO2(2) equimolar
Δ12 / 10-8 m2 s-1
Total pore concentration, ct / kmol m-3

Figure 24

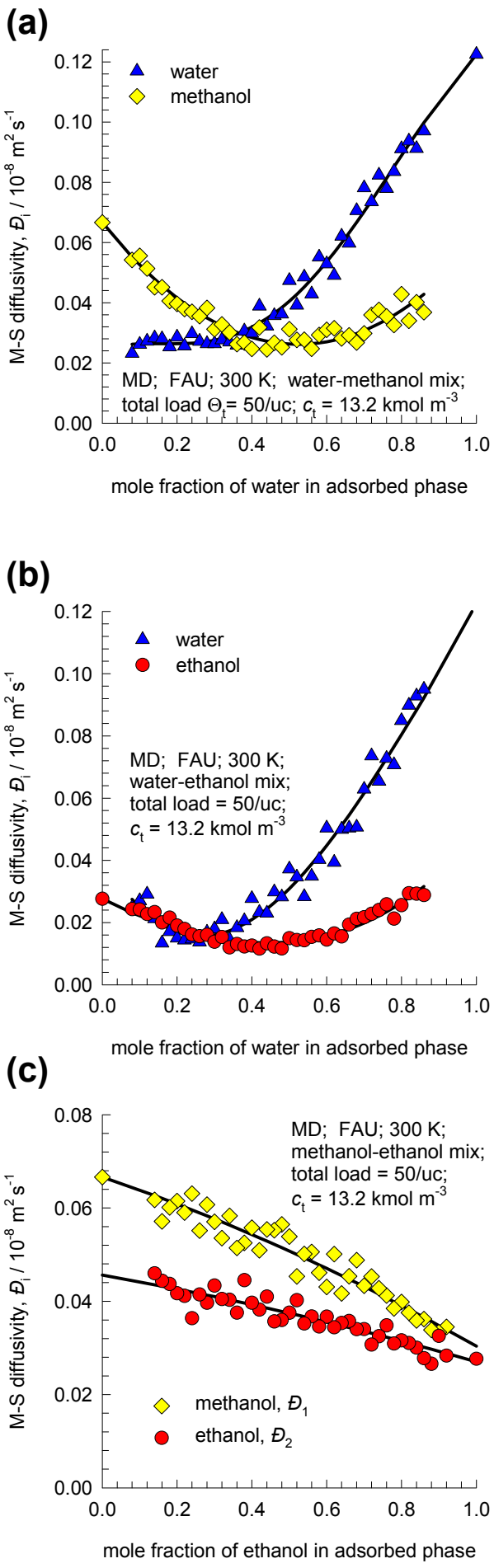
(a)
water
methanol
MD; FAU; 300 K; water-methanol mix;
total load Θt= 50/uc; ct = 13.2 kmol m-3
M-S diffusivity, Đi / 10-8 m2 s-1
mole fraction of water in adsorbed phase
(b)
water
ethanol
MD; FAU; 300 K;
water-ethanol mix;
total load = 50/uc;
ct = 13.2 kmol m-3
M-S diffusivity, Đi / 10-8 m2 s-1
mole fraction of water in adsorbed phase
(c)
MD; FAU; 300 K;
methanol-ethanol mix;
total load = 50/uc;
ct = 13.2 kmol m-3
methanol, Đ1
ethanol, Đ2
M-S diffusivity, Đi / 10-8 m2 s-1
mole fraction of ethanol in adsorbed phase

Figure 25

(a)

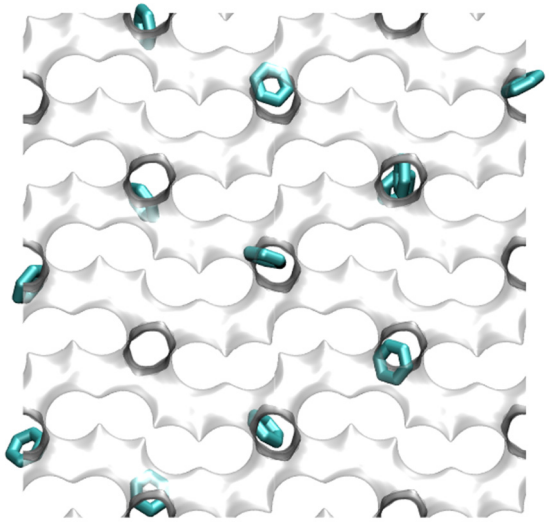

(b)

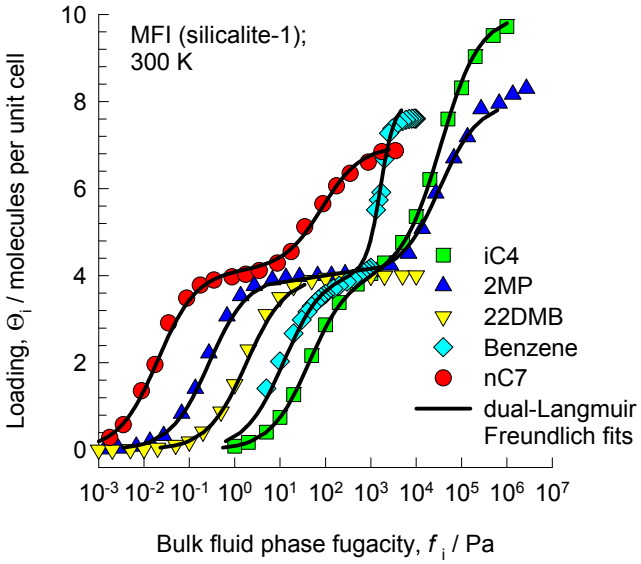
MFI (silicalite-1);
300 K
Loading, Θi / molecules per unit cell
0
2
4
6
8
10
10-3 10-2 10-1 100 101 102 103 104 105 106 107
Bulk fluid phase fugacity, f i / Pa
iC4
2MP
22DMB
Benzene
nC7
dual-Langmuir
Freundlich fits

Figure 26

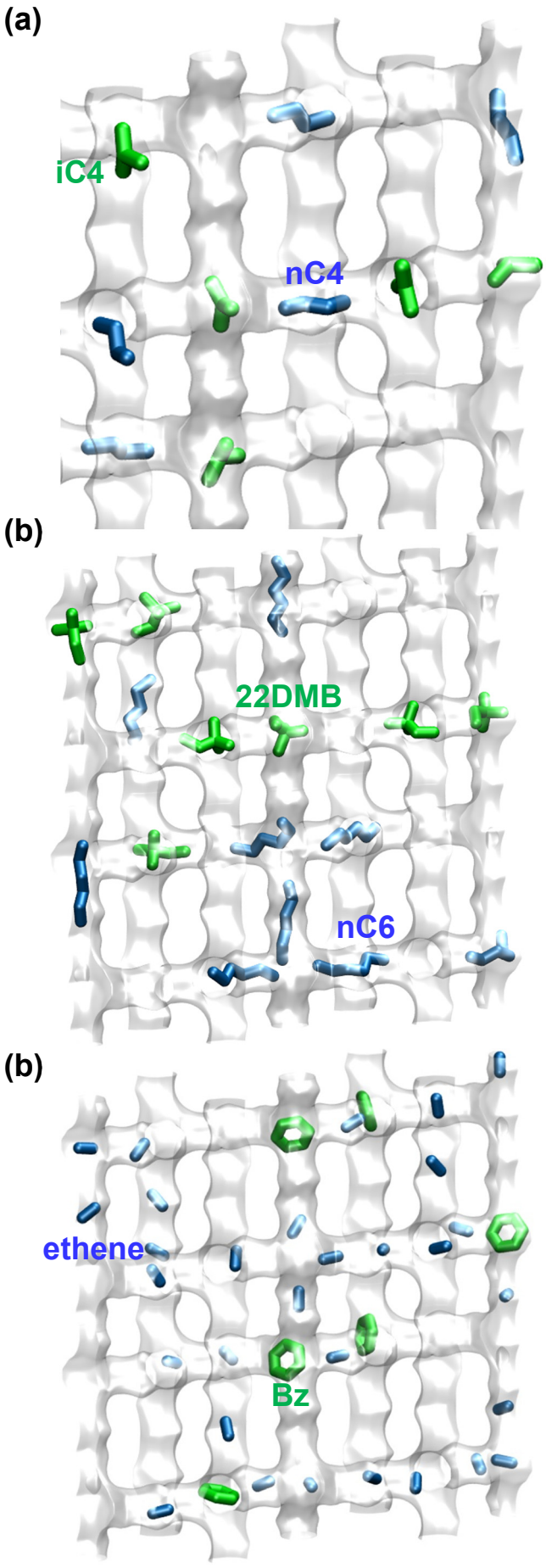

Figure 27

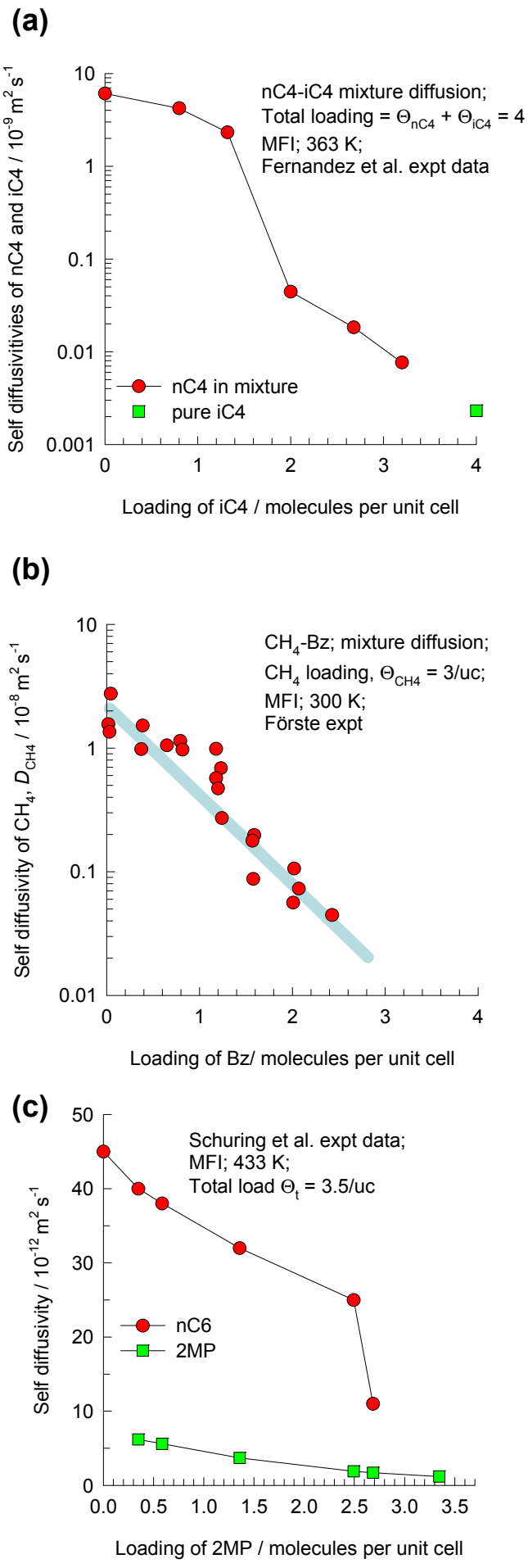
(a)
nC4-iC4 mixture diffusion;
Total loading = Θnc4 + Θic4 = 4
MFI; 363 K;
Fernandez et al. expt data
nC4 in mixture
pure iC4
Self diffusivities of nC4 and iC4 / 10-9 m2 s-1
Loading of iC4 / molecules per unit cell
(b)
CH4-Bz; mixture diffusion;
CH4 loading, ΘCH4 = 3/uc;
MFI; 300 K;
Förste expt
Self diffusivity of CH4, DCH4 / 10-8 m2 s-1
Loading of Bz/ molecules per unit cell
(c)
Schuring et al. expt data;
MFI; 433 K;
Total load Θt = 3.5/uc
nC6
2MP
Self diffusivity / 10-12 m2 s-1
Loading of 2MP / molecules per unit cell